J. Micromech. Microeng. **10** (2000) R9–R38. Printed in the UK PII: S0960-1317(00)06704-8

TOPICAL REVIEW

RF MEMS from a device perspective

J Jason Yao

Rockwell Science Center, M/S A23, 1049 Camino Dos Rios, Thousand Oaks, CA 91360, USA

E-mail: jjyao@rsc.rockwell.com

Received 14 March 2000, in final form 12 April 2000

Abstract. This paper reviews the recent progress in MEMS for radio frequency (RF) applications from a device perspective. RF MEMS devices reviewed include switches and relays, tunable capacitors, integrated inductors, mechanical resonators and filters, and some representative microwave and millimetre-wave components. Important device parameters are highlighted, as they have significant contributions to the performance of the final products in which the devices are used. The challenges and statuses of these RF MEMS devices are outlined and discussed. The intent of this topical review is to provide perspective to newcomers in the field, and empower potential end-users with an overall device picture, current status, and a vision of their ultimate performance capabilities.

(Some figures in this article are in colour only in the electronic version; see www.iop.org)

1. Introduction

Micro electro mechanical system (MEMS) is a technology that enables the batch fabrication of miniature mechanical structures, devices, and systems. The technology leverages existing state-of-the-art integrated circuit (IC) fabrication technologies and, hence, also exhibits many advantages indigenous to IC technologies. A few of those advantages include cost reduction through batch fabrication, device-to-device consistency from advanced lithography and etching techniques, and general performance advancements from dimensional downscaling, leading to a tremendous size and weight reduction. In addition, by using materials such as silicon and fabrication techniques compatible with IC technology, MEMS mechanical components can be made monolithically integrated with electronics, producing a complete and smart system-on-a-chip that interacts with the physical world, performs electronic computations, and communicates with other systems, if necessary. Silicon has been proven to be a suitable mechanical material for numerous applications at the reduced MEMS scale; dating back to 1982, its mechanical properties are well documented by Petersen [1]. These advantageous characteristics have positioned MEMS to be a winning technology in many application arenas, including accelerometers [2, 3], pressure sensors [4], micro-optics [5], and ink-jet nozzles [6]. Some are winning the battle against their conventional counterparts through device performance enhancements, others through manufacturing cost reduction. This paper reviews the general development of MEMS in another such technical area—MEMS for radio frequency (RF) applications or RF MEMS. More specifically, the paper will review a number of RF MEMS devices that serve as fundamental building blocks, including RF switches, tunable capacitors, high-Q inductors, high-Q mechanical resonators and filters, and some representative microwave and millimetre-wave components. Compared with other more mature MEMS technology fields, RF MEMS is relatively new, but has already generated a tremendous amount of excitement because both the performance enhancements and manufacturing cost reduction are evident characteristics of the technology. A topical review from a device perspective (as opposed to an application perspective) at this juncture should provide perspective to the newcomers in the field, and empower potential end-users with an overall device picture, current status, and a vision of their ultimate performance capabilities.

The modern commercial and especially military communications, navigation, data link, and avionics environment impose severe and often conflicting requirements on the electronics designed for these applications. In military communications applications, for example, there are typically multiple transmitters and receivers on the same platform (cosite) or nearby; there are also requirements for high-level anti-jam and the simultaneous use of multiple functions. For general communications systems in both commercial and military applications, there is a continuous movement to smaller, secure systems that have increased functionality and reduced power consumption. These demands place severe constraints on circuit power dissipation and electromagnetic compatibility (EMC), and significantly increase the equipment design complexity, manufacturing cost, and system weight in several ways. The presence of several transmitters operating simultaneously on the same platform with multiple receivers requires very high dynamic range receivers, ultra-clean transmitters, and careful attention to the overall EMC design of the system. This usually requires filtering on both transmitters and receivers to ensure that they do not interfere with

each other. The anti-jam requirements require a high degree of frequency agility to evade and lessen the impact of jamming signals on the desired communications. To fulfil these cosite requirements requires narrow band filtering on transmitters, receivers, or both. Highly frequency-agile filters for anti-jam requirements tend to be wider in bandwidth because it is difficult to use solid-state components to design and build highly selective filters with adequate agility. The current state-of-the-art circuit designs use a combination of many gallium arsenide (GaAs) FETs (field effect transistors), p–i–n (PIN) diodes, and/or varactor diodes to achieve the required switching, filtering, and tuning functions. The units fabricated using these components are characterized by high power consumption, low reliability, and high manufacturing cost. In addition, poor RF performances (e.g., more than 1–2 dB insertion loss per switching stage is typical in the solid-state approach) of these components introduce direct conflicts between the need to co-locate or cosite all of the frequency-agile communications functions for a given platform and the need for electromagnetic noise immunity. Additional gain is also required to be built into the system to compensate for the RF losses, thereby further raising power consumption, cost, and the system size and weight.

RF MEMS is a technology that addresses these shortcomings and offers the performance advantages of electromechanical components on size scales commensurate with single solid-state devices. In many cases, a single MEMS component replaces and outperforms an entire solid-state circuit. Although others do exist, and may be more sensible in a case-by-case situation, these are the general motivations for the development of RF MEMS. The advantageous characteristics of RF MEMS will become more apparent in the sections to follow.

There are many device parameters important in one application or another, and these parameters are often used as metrics to determine the performances of these devices. A selected set of these parameters is listed below with a brief qualitative definition. Because RF MEMS crosses the boundary between the electrical and mechanical world, some attention should be paid to these terms and definitions, as they can be confusing if not treated with care. The term quality factor, Q, has a similar definition in both electrical and mechanical domains, for example, but can refer to different aspects of a device for some (e.g., in an electromechanically tunable capacitor), and the same aspect of a device for others (e.g., in a mechanical resonator). As another example, the switching speed of an RF switch sometimes is highlighted by its mechanical resonant frequency (typically sub-megahertz), which can be confused with, but in most cases is different from, the electrical signal frequency the device carries (which may be gigahertz and beyond). A clear differentiation between these and other parametric terms crossing the electrical–mechanical boundary is thus in order.

The *insertion loss* of an RF switch refers to the RF loss dissipated in the device, typically characterized by S21 between the input and output of the switch in its pass-through state, which is the closed state for a series switch. The main contributing factors include resistive loss due to the finite resistance of the signal lines and contact at low to medium frequencies, and loss due to the skin depth effect at high frequencies.

The *return loss* of an RF switch refers to the RF loss reflected back by the device, typically characterized by S11 at the input of the switch in its pass-through state. The main contributing factors include the mismatch of the switch's total characteristic impedance.

The *isolation* of an RF switch refers to the RF isolation between the input and output, typically characterized by S21 of the switch in its blocking state, which is the open state for a series switch. The main contributing factors include capacitive coupling and surface leakage.

The *linearity* of an RF component refers to the independence of device impedance from the input RF signal power, typically characterized by the third-order intersecting point, or IP3, in a two-tone RF intermodulation measurement.

The *equivalent series resistance* of an RF reactive component refers to the equivalent resistance, R, in the reactive component that is being modelled as a simple series configuration between R and pure imaginary impedance, Z_{im}, where Z_{im} is $1/(\mathrm{j}\omega C)$ for a capacitor, and $\mathrm{j}\omega L$ for an inductor.

The *quality factor*, Q, can be generally defined for both electrical and mechanical components as the ratio of the energy stored in a device to the energy dissipated per cycle of resonance. For an *electrical* reactive component, Q is typically expressed as the ratio of the imaginary portion of the impedance to its real portion.

The *resonant frequency* of a device generally refers to the particular frequency at which the stored kinetic and potential energy resonates. For a simple electrical system like an LC tank, the fundamental resonant frequency is $[1/(2\pi)]\sqrt{1/(LC)}$. For a simple mechanical spring–mass system, the fundamental resonant frequency is $[1/(2\pi)]\sqrt{k/m}$, where k is the spring constant of a mass-less spring and m is the resonating mass without compliance.

2. RF switches

With batch fabrication, MEMS switches or relays have overcome one of the major manufacturing shortcomings of their conventional macroscopic mechanical counterparts, both in cost reduction and in integration compatibility with electronics. Micromechanical switches or relays were among the first devices studied in the MEMS field. Petersen reported a membrane-based switch on silicon as early as 1979 [7]. Since then, a large number of journal and conference papers have been published on the MEMS switch subject with various actuation designs including electromagnetic [8–11], magnetostatic [12], electrostatic [13], thermal–electric [14], and various structural designs including a rotating transmission line [15], surface micromachined cantilevers [16–25], multiple-supported or membrane based designs [16, 18, 26–31], bulk micromachined or wafer bonded designs [32–34], diamond cantilever and contact [35], polysilicon switch [36], mercury micro-drop contact [37, 38], and bistable microrelays [39, 40]. Lateral contacting switches [41, 42] have also been studied. Their dynamic behaviour shows promising characteristics, superior to many of the vertical contacting switches. However, their contact mechanisms are very inferior to that of a vertical contacting switch, due to

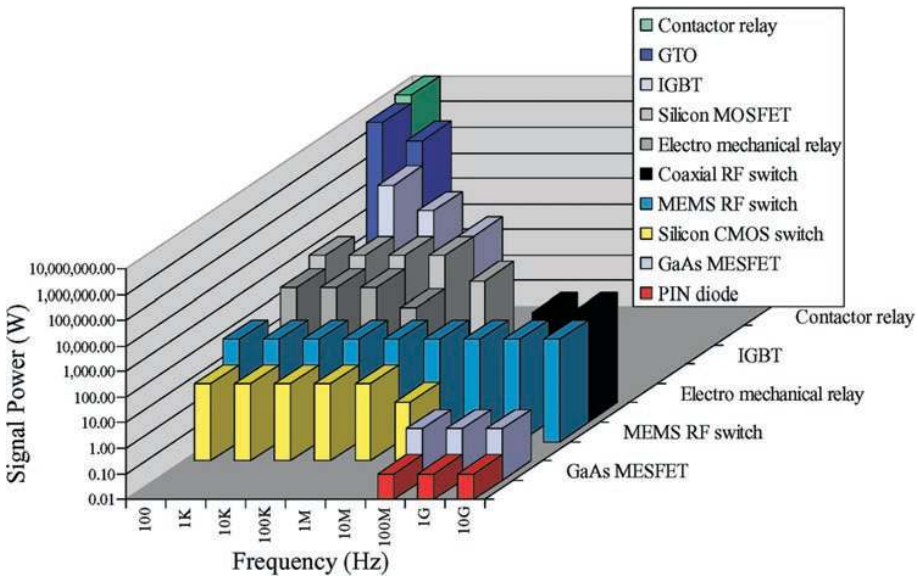

Figure 1. A qualitative illustration of switch technology usage for signal power levels from milliwatts to megawatts and a frequency spectrum from tens of hertz to tens of gigahertz.

the roughness in etched side-surfaces and contact materials [41]. Similar to the lateral contacting switch, all switch designs have their advantages and disadvantages; the tradeoff between the two and the final design selection, in most cases, is heavily guided by their targeted applications. In general terms, cantilevered and multiple-supported surface micromachined electrostatic switches or relays are by far the most widely studied devices to date. The electromechanical behaviours of these electrostatic switches are similar, and an example analysis was presented by Grétillat *et al* in 1997 [43]. The main attraction behind this device design is its low actuation power consumption (zero static current) and its integration compatibility with various electronic IC platforms. As for general applications, although others, such as automotive and switching power supply, do exist, major applications of MEMS switches include automatic test equipment (ATE) [34] and RF communications.

Electrical switches are widely used in the communications industry. Common applications include signal routing, impedance matching networks, adjustable gain amplifiers, etc. The communication frequencies cover a broad range from the below-a-megahertz AM band, to the commercial FM band (88–108 MHz), to various military hand-held radio transceivers up to approximately 400 MHz, and to the cellular frequencies of around 900 MHz and 2.4 GHz. In addition, there are also other applications in the microwave and millimetre-wave regimes, ranging from the low X-band to the high side in the W-band, that require the use of high-quality switches. State-of-the-art switch technology uses solid-state semiconductor devices for their integration compatibility and relatively lower manufacturing cost attributed to batch fabrication. With the conventional approach, the wide frequency spectrum of communications calls for different switch technologies for different frequency applications. Application requirements also vary to a large degree. Some are more forgiving where manufacturing costs would then be the main focus; others are extremely stringent where switch performance is the primary consideration and the type of switch technology used becomes much less significant. Figure 1 qualitatively illustrates some switch technology usage including, simply for comparison, some devices that are not typically used for communications applications. The signal frequency and power handling capability are the two parameters used in this example of a device-to-device comparison. It should be noted that these two parameters are by no means the only parameters of importance for a switch. Some switches, such as silicon FETs, can handle a high level of signal power at low frequency, but the performance drops off dramatically as frequency increases; others, such as GaAs metal–semiconductor field effect transistors (MESFETs) [44–46] and PIN diodes [47], work fairly well at high frequency, but handle minimal signal power level. Overall, however, when the signal frequency becomes greater than 1 GHz, these solid-state switches have a large insertion loss (typically 1–2 dB) in the pass-through state and a poor electrical isolation (typically on the order of −20 to −25 dB) in the blocking state. The need for an alternative replacement is inevitable and MEMS exhibits promising characteristics as the new technology for integrated switching devices.

From a switch contact perspective, there are two types of switches based on the MEMS technology—metal contacting [16] and capacitive coupling [28]. The metal contacting switches, as illustrated in figure 2, use metal-to-metal direct contact to achieve an ohmic contact between two electrodes. This ohmic contact characteristic allows the device to be suitable for low-frequency applications including dc, as well as high-frequency applications. The broad frequency coverage of MEMS metal contacting switches is a major advantage of the technology, as highlighted in figure 1. The tradeoff is in its contact lifetime, which is a common shortcoming of all metal contacting mechanical switches. Nevertheless, the typical lifetime of 100 000 000 cycles [26] is already adequate for some applications. An example is demonstrated in [26] where MEMS switches are

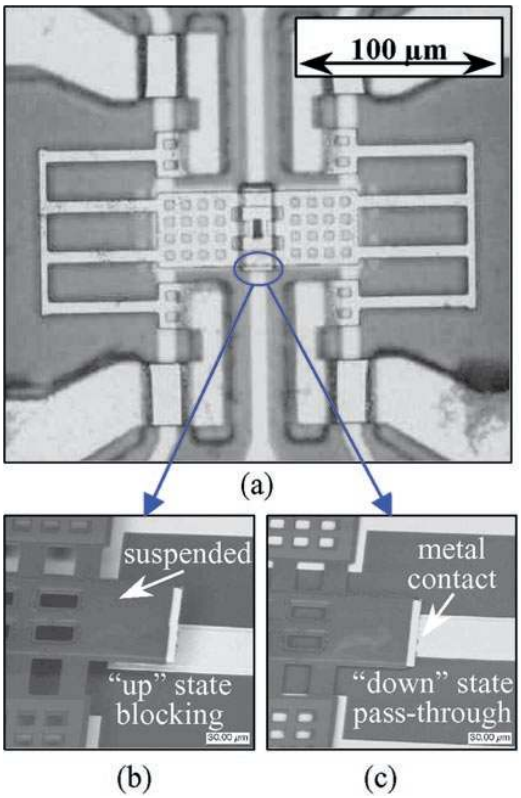

Figure 2. The RSC metal-to-metal contact MEMS switch with (a) a top-view shown, and higher magnification perspective views shown in its (b) 'up' blocking state and (c) 'down' pass-through state.

monolithically integrated with GaAs pseudomorphic high electron mobility transistor (PHEMT) low-noise amplifiers (LNA), as illustrated in figure 3. The MEMS switches are used for signal routing between two LNAs with different frequency characteristics. The amplifier gains selected by the integrated MEMS switches are plotted in figure 4. The capacitive coupling switches, as illustrated in figure 5 [28–30], have a thin dielectric film and an air gap between the two metallic contact surfaces. The air gap is electromechanically adjusted to achieve a capacitance change between the 'up' and 'down' state. The capacitance ratio of the downstate value to the upstate value is a key parameter for such a device; a high capacitance ratio is always desirable. Because of the capacitive coupling nature, in most cases these switches are not suitable for low-frequency applications. However, the contact lifetime is typically a smaller issue compared with that in a metal contacting switch.

Alternatively, MEMS switches can also be catalogued into another two types from an application perspective—serial and shunt switches, as illustrated schematically in figure 6. Although both metal contacting and capacitive coupling switches can be used as either a serial or a shunt switch, metal contacting switches are often used as serial switches, while capacitive coupling switches are used for shunt switches. The advantage and disadvantage comparison between the two ways of using the switches is primarily within the RF circuit design, rather than MEMS switch components. The final design selection is heavily guided by specific applications.

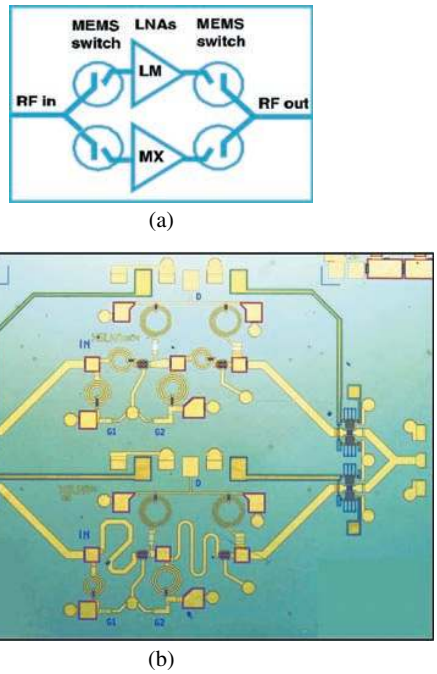

Figure 3. (a) A schematic circuit diagram and (b) a micrograph of the fabricated circuit with MEMS RF switches monolithically integrated with PHEMT LNAs (from [26], RSC).

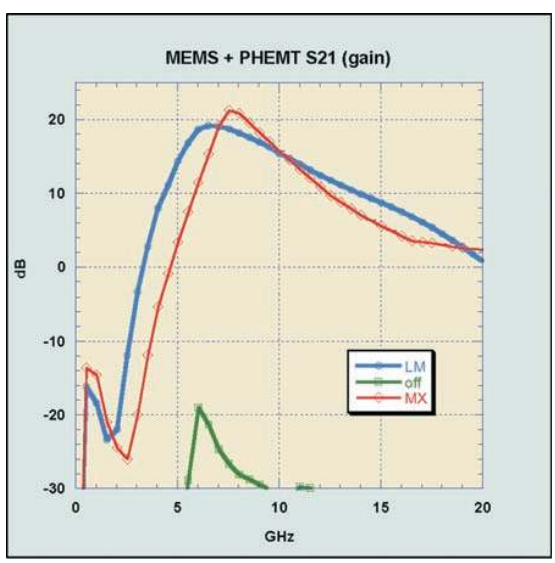

Figure 4. Amplifier gains of the circuit shown in figure 3 are selected by the integrated RSC MEMS switches, and are plotted up to 20 GHz (from [26], RSC).

2.1. Metal contacting serial switch

The example of a metal contacting serial switch, as shown in figure 2, was developed at the Rockwell Science Center (RSC) [16, 26]. The switch uses a coplanar waveguide (CPW) design with a ground–signal–ground parallel metal line configuration of specific dimensions that, along with the substrate material properties, result in a constant characteristic impedance of choice—50 Ω in this example. There is a gap in the signal line that separates the input and output signal terminals. Suspended above the gap is a metal shunt bar, as can be seen in figure 2(b). This metal shunt

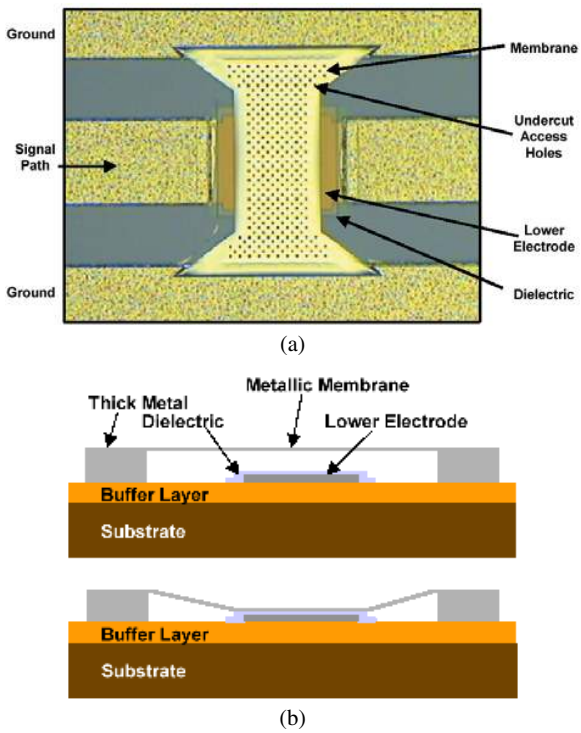

Figure 5. (a) A micrograph and (b) a schematic cross sectional illustration of a capacitive coupling MEMS RF switch (from [28–30], Raytheon/Texas Instruments (TI)).

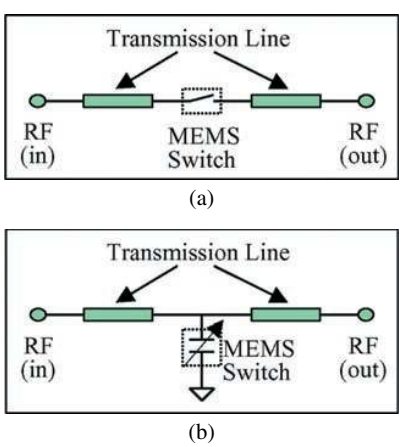

Figure 6. A schematic illustration of (a) a serial switch configuration and (b) a shunt switch configuration.

bar is attached through an insulating silicon dioxide (SiO_2) film to the also suspended drive plates. A double-folded SiO_2 spring structure is used to support the drive plates and, hence, the metal shunt bar. As an electrostatic voltage is applied between the drive plates and the ground electrodes underneath, an electrostatic force is created to pull the entire suspended structure downward to the substrate, as shown in figure 2(c). This actuation causes the metal shunt bar to make an electrical contact to the two metal signal lines across the gap and completes the switching circuit. The entire switch, excluding bond pads, occupies a nominal area of 80 μm by 160 μm.

The RSC switch is manufactured using a surface micromachining technique with a total of five basic

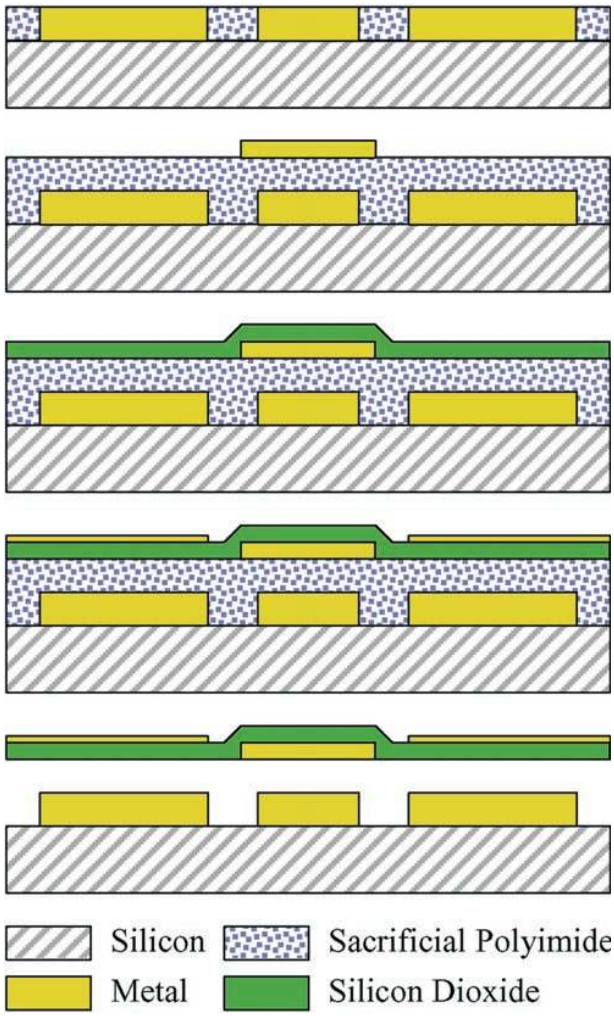

Figure 7. An abbreviated schematic process illustration showing the device cross sections at key processing steps for making a RSC MEMS RF switch.

masking levels. SiO_2 deposited using a plasma enhanced chemical vapor deposition (PECVD) technique is used as the structural material, and polyimide is used as the sacrificial material. Figure 7 is an abbreviated cross sectional schematic illustration of the process sequence, details of which are described in [16]. The entire process stays below 250 °C, ensuring the RF switch's monolithic integration compatibility with microwave and millimetre-wave integrated circuits (MMICs). As in most low-temperature surface micromachining processes, the starting substrate does not influence the outcome of the process to first order. Semi-insulating GaAs wafers are typically used as the substrate for the RSC switches, although other materials, such as silicon and glass, have also been used. The RF path in this metal contacting switch is electrically isolated from switch control lines using the SiO_2 material, and the switch structure is released by dry etching of the sacrificial polyimide film in an oxygen plasma. Dry release is preferred over wet chemical releasing methods to prevent any potential sticking problems during release.

The contact material for a microswitch is typically gold based for its noble nature, superior conductivity, and

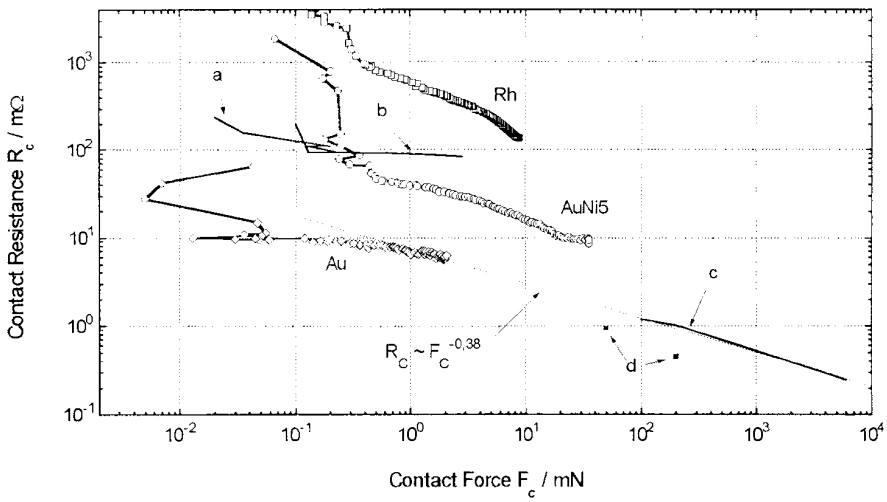

Figure 8. Contact resistances of AuNi5 and Rh are compared with that of Au with respect to the contact force (from Schimkat [48]).

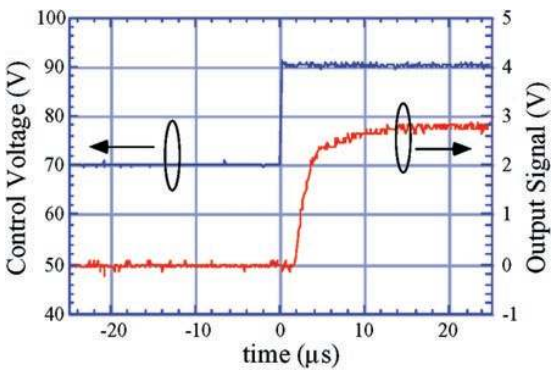

Figure 9. Transient response of the RSC MEMS switch with an input signal of 2.8 V dc. A switching time of 4 μs is achieved with no signal bouncing.

its compatibility with MMICs. Materials, such as AuNi5 and Rh, have been studied by Schimkat [48] as material candidates for microswitch contact, and compared with Au with respect to the contact force, as illustrated in figure 8 [48]. The contact material selection must be carried out with careful consideration of, and a balance among, a number of key switch parameters including contact resistance, metal sticking behaviour, lifetime, and environmental and packaging compatibility. In general, microswitches can benefit from an increased contact force, which has led to numerous research developments in large-force actuator designs, such as the thermal buckling actuator by Seki *et al* [49]. However, most higher power actuators also consume more power for actuation. Another tradeoff needs to be kept in mind.

Some of the performance characteristics of the RSC metal contacting serial switch are listed here, and will be discussed in more detail in the switch comparison section below. The typical switching time is less than 4 μs with no signal bouncing, as shown in figure 9. The actuating pull-down voltage is about 60 V on average, although various designs can have pull-down voltages ranging from 28 V [16] to 90 V. Insertion losses in the 'on' or pass-through state are typically ∼0.2 dB from dc to 40 GHz, and

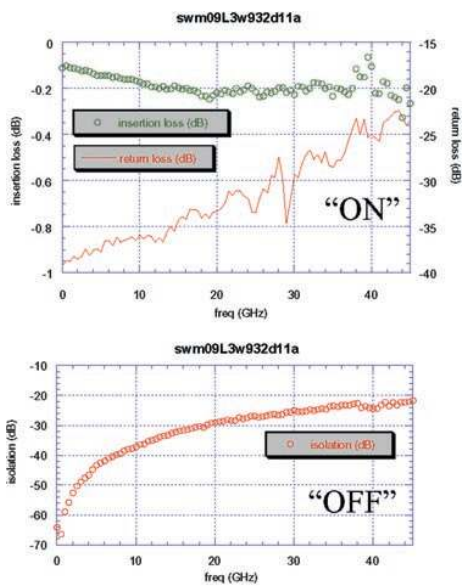

Figure 10. RF performances of the RSC MEMS switch showing low losses and high isolation from low frequency to 50 GHz.

isolation in the 'off' or blocking state is very high, about −60 dB, at low frequencies around 1 GHz or below, and decreases with increasing signal frequency to about −25 dB at 40 GHz (figure 10). Switch lifetimes of 100 000 000 cycles cold-switched (zero signal) and 10 000 000 cycles hot-switched (1–40 mA through the contact) have been demonstrated [26]. Linearity has been characterized for a number of RSC switches using two-tone measurement techniques. Measurements at tone frequencies near 112 MHz with a tone separation of 200 kHz reveal a third-order intermodulation product, IP3, of approximately +55.75 dBm [50]. The PIN diode that the MEMS switch is replacing only has an IP3 of +28 dBm.

2.2. Capacitive coupling shunt switch

An example of a capacitive coupling shunt switch was developed at Texas Instruments (TI) (now a part of Raytheon)

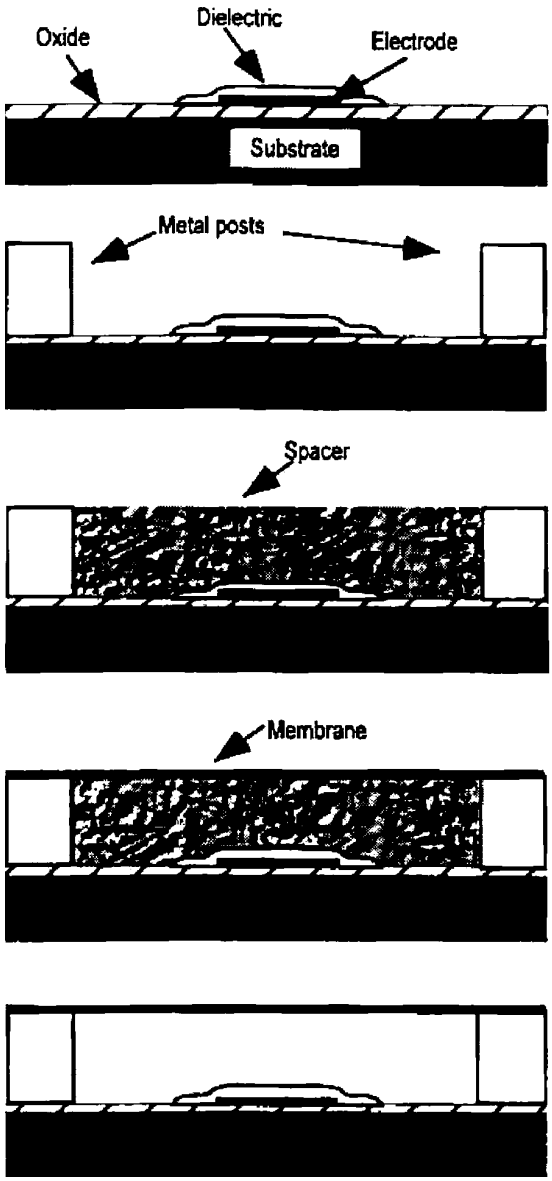

Figure 11. A schematic process illustration showing the device cross sections at key processing steps for making a TI MEMS RF switch (from [30], Raytheon/TI).

[28–30]. This switch also uses a CPW design with a ground–signal–ground configuration. A micrograph of this TI membrane switch is shown in figure 5. The switch has dimensions of about 120 μm in width and 280 μm in length, and consists of a thin aluminium alloy membrane suspended over a dielectric film deposited on top of the bottom electrode. In the membrane up state, or the pass-through state, most of the RF signal passes through the CPW signal line with a minimal capacitance C_{off} on the order of 35 fF between the bottom signal line and the suspended aluminium membrane. When an electrostatic voltage of the order of 50 V is applied between the membrane and the bottom electrode, an electrostatic force is created to attract, or pull, the membrane down onto the dielectric film on top of the bottom electrode, as illustrated in figure 5(b). This configuration increases the coupling capacitance C_{on} between the signal line and the grounded membrane to about 2.1–3.5 pF, resulting in an on–off capacitance ratio approximately between 60 and 100. The increased capacitance in the down state, or the blocking state, of the membrane switch creates a small impedance between the signal line and the ground, and thus blocks the RF signal from passing through to the other side of the signal line.

The TI switch is manufactured using a surface micromachining technique with a total of five masking levels and a high-resistivity (>5000 Ω cm) silicon wafer as the starting substrate material. Figure 11 is a cross sectional schematic illustration of the essential process sequence. Details of this fabrication process are illustrated in [30]. A thin layer of high-melting point W film (<0.5 μm) is used as the bottom electrode; an aluminium alloy film is used to form the suspended membrane structure; and photoresist is used as the sacrificial layer, which is consequently removed in an oxygen plasma for the switch structure release.

The ratio between C_{on} and C_{off} is a key parameter for the capacitive coupling shunt switch as it is a determining factor for both insertion loss and isolation. A small C_{off}, required for maintaining low insertion loss, requires a large gap between the membrane and the bottom electrode, which is a tradeoff with achieving a low pull-down voltage. A large C_{on}, required to maintain high isolation, requires an intimate contact between the membrane and the dielectric film over the bottom electrode in the switch's blocking or down state. Hillocking in low-melting-temperature metallic film during a relatively high-temperature processing step, such as silicon nitride deposition at 300 °C, and polymer residues from incomplete sacrificial photoresist removal, can all be potential causes for air gap formation between the two surfaces. A high-melting temperature film such as W is thus used to avoid hillocking. The stress level within the membrane film can also affect the performance of the switch. A low-tensile-stressed material is preferred because high-tensile-stressed material can increase the pull-down voltage, while compressive-stressed material may cause the membrane to buckle.

Some of the performance characteristics of the TI capacitive coupling shunt switch [30] are listed here, and will be discussed in more detail in the switch comparison section below. The typical switching time is on the order of 3.5–5.3 μs, as shown in figure 12. The actuating pull-down voltage is about 50 V. Insertion losses in the pass-through or up state are 0.15 dB at 10 GHz and 0.28 dB at 35 GHz, as illustrated in figure 13. Isolation is about −15 dB at 10 GHz and −5 dB at 35 GHz, as illustrated in figure 14. A switch lifetime of 500 000 000 cycles has been demonstrated [30].

2.3. Characteristics and performances of RF switches

As mentioned in a previous section, a large number of RF switch parameters exists with various levels of importance in various applications, and often with conflicting requirements. Tradeoffs among them and the final device selection are heavily guided by the targeted applications. Brown published a paper in 1998 [51] with a good comparison of RF switches for re-configurable ICs, such as quasi-optical beam steering and electrically re-configurable antennae. However, a comparison of *all* existing MEMS switches and relays for *general* RF applications would be an extremely challenging

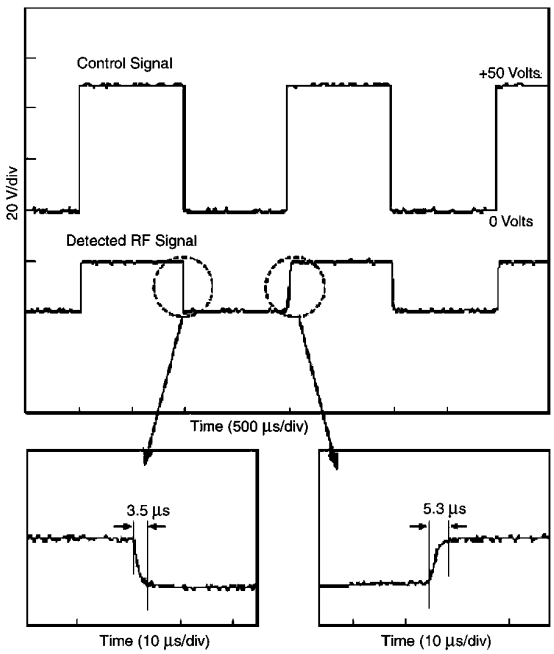

Figure 12. Switching time of the TI capacitive coupling shunt switch is of the order of 3.5–5.3 μs (from [30], Raytheon/TI).

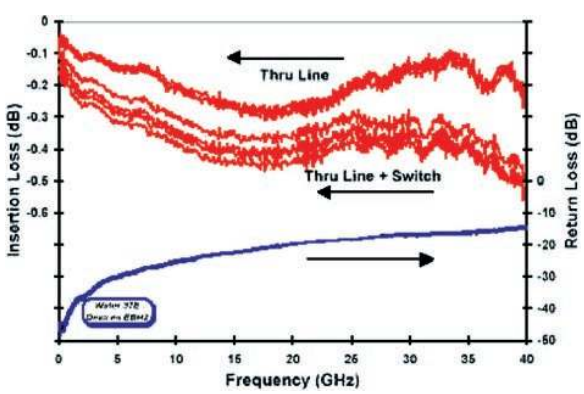

Figure 13. Insertion losses (of four switches) and return loss of the TI membrane switch are illustrated up to 40 GHz (from [30], Raytheon/TI).

task, if at all possible. Instead, representative characteristics and device performance parameters of a selected number of MEMS switches are tabulated in table 1, and the comparison among these switches will be left to the readers and the potential users of these devices. Average FET switches based on GaAs MMIC technology are used as the baseline device. MEMS switches and relays listed in table 1 include devices by the RSC (figure 2) [16, 26], TI (now a part of Raytheon) (figure 5) [28–30], HRL Laboratories (figure 15) [19, 20], University of Michigan (figure 16) [27], Northeastern University (figure 17) [21–23], Siemens AG (figure 18) [24], OMRON (figure 19) [32], and NEC (figure 20) [25]. It should be noted that, due to space limitation, some of the MEMS switches are not listed here, and they should *by no means* be considered inferior because of their absence.

The MEMS switches in table 1 have different dimensions ranging from just below 100 μm to slightly over 2 mm.

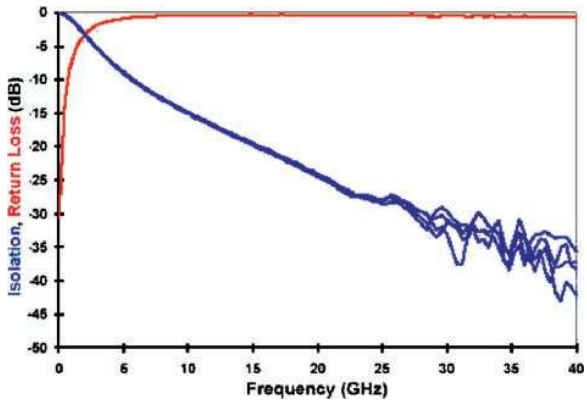

Figure 14. Typical isolation and return loss of the TI membrane switch are illustrated up to 40 GHz (from [30], Raytheon/TI).

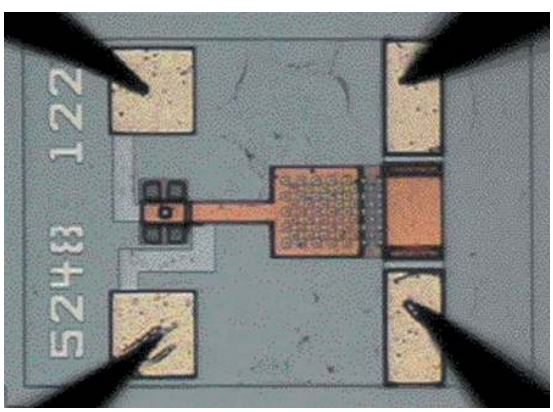

Figure 15. A micrograph showing the top-view of a HRL MEMS cantilever switch (from [20], HRL Labs).

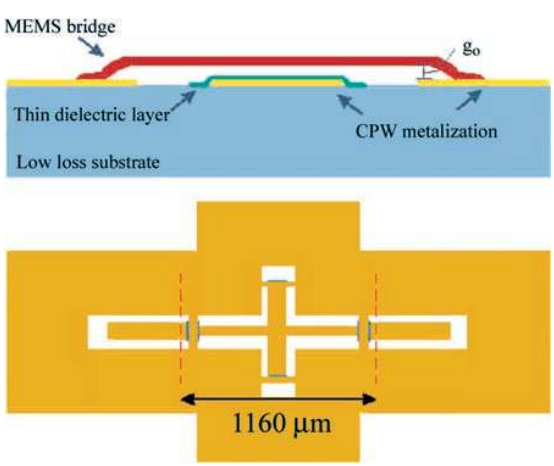

Figure 16. A schematic illustration showing the cross section (top) and a layout of a University of Michigan MEMS cross switch (from [27], University of Michigan).

However, they all represent a single switch device with the exception of the University of Michigan device, which consists of four switches, but performs one single switching function. The RF signal power level that each device is capable of handling is an important parameter of the device. However, that parameter has rarely been reported, primarily because the test set-up requires a relatively expensive high-power RF generator. Therefore, a maximum dc current level

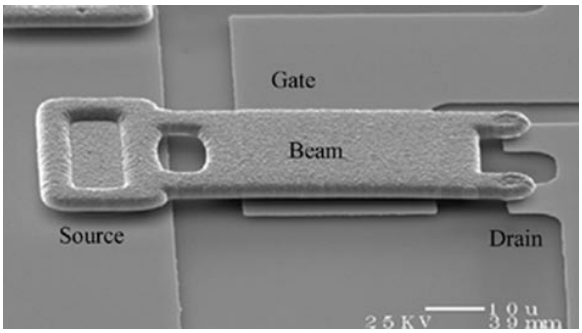

Figure 17. SEM micrograph of a Northeastern University MEMS switch (from [23], Northeastern University).

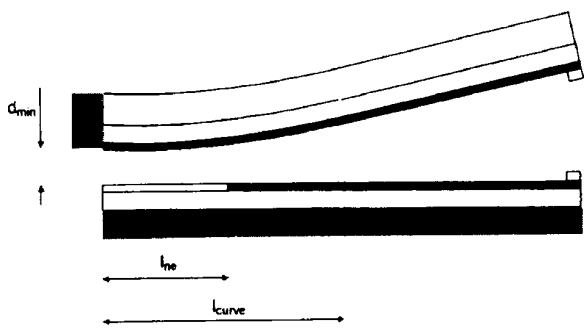

Figure 18. A cross sectional schematic illustration of the Siemens MEMS relay (from [24], Siemens AG).

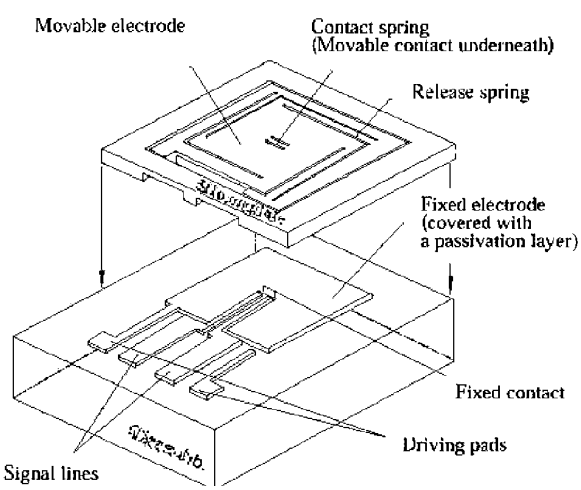

Figure 19. An exploded view of the OMRON MEMS relay (from [32], OMRON).

that each device is capable of handing is listed instead as a less-than-ideal indication of the RF power capacity.

At low frequency, the 'on' resistance in the pass-through state and 'off' resistance due to leakage in the blocking state are the two main electrical criteria for a switch. However, at high frequency, the associated inductance in the pass-through state becomes a significant factor in addition to losses other than resistive loss, such as that caused by the skin depth effect, since RF signals travel only on the surface of a metallic conductor. When the skin depth effect is the dominating loss mechanism, the surface area and metal conductivity become the key factors, as opposed to the cross sectional area and the total metal conductance. The coupling and

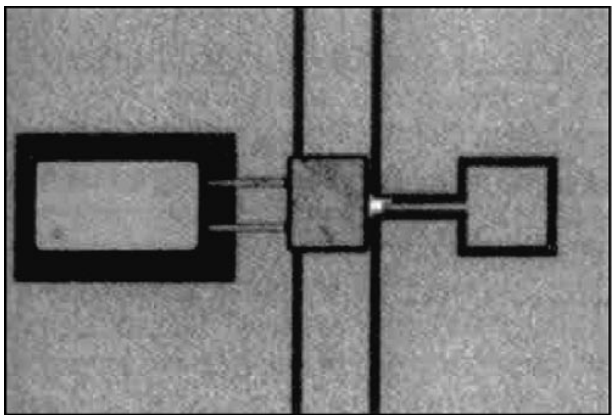

Figure 20. A micrograph of a NEC MEMS switch (from [25], NEC).

parasitic capacitance in the blocking state can also couple the RF signal through the blockage, in addition to leakage pathways. Thus, the electrical performance of a switch at high frequencies should be characterized by its insertion and return losses in the pass-through state and isolation in the blocking state. 'On' and 'off' resistance is used only when the insertion loss and isolation parameters are not available for certain switches in table 1.

Another important parameter is the switch lifetime, which is often measured in a number of different ways depending on the requirements of the targeted applications. The most basic lifetime measure is the mechanical lifetime of a switch achieved by examining the degradation (or the lack of it) of the mechanical structure excluding the switch's contact behaviour. However, contact is a major part of a switch, and should be included as it often contributes significantly to the failure of a switch. When contact is included in lifetime studies, there are also cold-switched and hot-switched lifetimes. Cold-switching refers to the opening and closing of a switch with zero signal level through the contact, while hot-switching refers to that of a switch with a specified signal level through the contact and often also a specified loading type, for example resistive, inductive, etc. A switch lifetime can differ a great deal based on different switching conditions. Hence, what is being reported in a technical paper on the subject of a switch's lifetime often varies based on the different requirements of their targeted applications. For general RF applications, hot-switched lifetime with a certain RF signal level passing through the contact is most informative. However, such experiments would monopolize a number of pieces of expensive RF equipment that are often in heavy demand at a typical research and development laboratory: dc or low-frequency signals are frequently used in a hot-switched lifetime experiment instead.

3. Tunable capacitors

Another component that is widely used for its tuning functionality in RF communications applications is the tunable capacitor, or varactor. Applications include low-noise parametric amplifiers, harmonic frequency generators, and frequency controllers, such as voltage-controlled oscillators (VCO). Conventional solid-state varactors are

Table 1. Characteristics and performances of selected MEMS RF switches. Note, for the FET switch average GaAs MMIC FET switches are used for comparison.

Device characteristics and performance parameters	FET switch	Rockwell (RSC) [16, 26]	Raytheon/TI [28–30]	HRL Labs [19–20]	University of Michigan [27]
MEMS technology	—	Surface	Surface	Surface	Surface
Device size (μm × μm)	∼1 mm^2	80 × 160	120 × 280	∼120 × 300	∼1000 × 2000[a]
Current handling (mA)	∼200	200	Not available	140	Not available
Structural material	GaAs	SiO_2	Al alloy	Si_xN_y	Plated Au
Actuation mechanism	—	Electrostatic	Electrostatic	Electrostatic	Electrostatic
Actuation voltage (V)	∼1	∼60	∼50	∼25	15–20
Contact mechanism	Semiconductor	Au based metal	Capacitive	Au	Capacitive
Insertion loss (dB)	2 at 6 GHz	0.2 (dc–40 GHz)	0.15 at 10 GHz 0.28 at 35 GHz	0.2 (dc–40 GHz)	0.6 (22–38 GHz)
Isolation (dB)	−22 at 2 GHz −20 at 6 GHz	−32 at 10 GHz −22 at 40 GHz	−15 at 10 GHz −35 at 35 GHz	−40 at 12 GHz −27 at 40 GHz	−40 at 22 GHz −50 at 35 GHz
Switching time	10 ns	2–5 μs	3.5–5.3 μs	20 μs	Not available
Lifetime (million cycles)	>100 000	∼100 (cold) 10s (hot 1–40 mA)	500	∼4 (hot 10 mA)	Not available
Others	Values may vary from device to device	third order IM product 71.5 dB below tone level	IP3 > +66 dBm	Unidentified resonance at 8.5 GHz	Tuned for 30 GHz performance

Device characteristics and performance parameters	Northeastern University [21–23]	Siemens AG [24]	OMRON [31]	NEC Corporation [25]
MEMS technology	Surface	Bulk	Bonded wafer	Bonded wafer
Device size (μm × μm)	Beam = 30 × 65	1.5 (mm^2)	2000 × 2500	250 × 900
Current handling (mA)	150	>100	Not available	Not available
Structural material	Au/Ni	Silicon epi	Silicon	P++ Silicon
Actuation mechanism	Electrostatic	Wedge electrostatic	Electrostatic	Electrostatic
Actuation voltage (V)	30–300	24	16–19	125
Contact mechanism	Au	Plated Au alloy	Au	Au
Insertion loss (dB)	Not available dc $R \sim 0.1$–10 Ω	Not available dc $R < 5$ Ω[b]	Not available dc $R \sim 0.5$ Ω	0.2 at 30 GHz
Isolation (dB)	Not available	Not available dc $R > 100$ GΩ	Not available	−13 at 30 GHz
Switching time	150 kHz cutoff	<0.2 ms	<0.3 ms	—
Lifetime (million cycles)	0.01–1000[c] (cold)	Not available (mechanical life 100)	1–10 (hot 10mA)	—
Others	500 million cycles for N_2 packaged hot-switch at 10 mA	Contact force is of the order of 1 mN	5 mN contact force Lifetime uses resistive load w/10 V	Double-hump design is used above

[a] Including four membrane switches to form a cross switch with short transmission lines.
[b] Including feed line resistance.
[c] Cold-switching lifetime depends on number of contacts ranging from 8 to 64.

made in silicon or gallium arsenide using either p–n or Schottky-barrier junction structures. Several figures of merit used in association with tunable capacitors include unbiased base capacitance; tuning ratio; equivalent series resistance or quality factor, Q; associated inductance or electrical self-resonance; and device linearity in response to RF power. The value of the unbiased base capacitance depends on the circuit requirements of a specific application and the frequency the tunable capacitor is used for. Typical values range from tens of picoFarads for very-high-frequency (VHF) applications to about 0.1 pF for applications approaching the X-band. For frequencies at the X-band and beyond, lumped-element approaches are mostly replaced by distributed-element or microwave approaches. Therefore, passive components such as the tunable capacitor are rarely used at those high frequencies. The tuning ratio is a parameter that is often found to be a limiting factor in RF circuit design. Although some applications require only a small tuning range (about tens of per cent) to fine adjust an impedance value, most applications call for a large tuning ratio in excess of 2:1. In fact, frequency-hopping secured communication units, for example, often spread over octaves, and can only be constructed with multiple modules sectioned in the frequency domain. Among others, the lack of tuning range of the existing solid-state tunable components is a key factor behind this less-than-optimal design solution. Another critical figure of merit in a tunable capacitor is the equivalent series resistance, which in many cases is the determining factor of the device's quality factor, Q. If other loss factors are negligible when compared to resistive loss, Q can then be expressed as follows:

$$Q = \frac{1}{\omega C R}. \tag{1}$$

The larger the resistance, the smaller the Q, and also the greater the resistive loss for the device. In an imperfect real world where the equivalent series resistance, R, cannot be eliminated totally, one would at least keep it low enough

such that the resulting Q of the tunable capacitor would be greater than that of other components used in the same circuit. For example, let us assume that one wants to use a discrete inductor along with a tunable capacitor to form a tunable resonating LC tank that nominally centres at 100 MHz. Let us further assume that the best discrete inductor that one can find has a Q value of 50 at that particular frequency. The equivalent series resistance, R, of the tunable capacitor thus would need to be much less than $1/(\omega C Q)$ in order to avoid imposing any significant additional loss on the circuit. For a capacitance value of 10 pF at 100 MHz, the term $1/(\omega C Q)$ in this example comes to 3.18 Ω, and only a small percentage of this number (e.g., <1 Ω) may be acceptable as the equivalent series resistance. Coincidentally, an equivalent series resistance of less than 1 Ω is a quite common requirement for many applications in VHF and ultra-high-frequency (UHF) regimes. Based on this simplified exercise, one can readily calculate the maximum equivalent series resistance tolerable to a circuit. The Q requirement places significant challenges on solid-state varactors. A common practice is to boost Q when it is absolutely necessary by connecting the varactor in series with a smaller and much higher *Q fixed* capacitor. The overall capacitance is then dominated by the smaller fixed capacitor while the overall resistance is still mainly contributed by the varactor, since the fixed capacitor has a much higher Q. The end result is the overall Q of this serial configuration is increased by approximately a factor of the capacitance of the varactor over that of the smaller fixed capacitor. However, the tradeoff is significant. Because the smaller fixed capacitor dominates the impedance of the overall configuration, the tuning ratio will be reduced dramatically by approximately the *square* of that capacitance-ratio factor.

Another parameter in the set of figures of merit described here is the inductance associated with a tunable capacitor. Like trying to eliminate the equivalent series resistance, eliminating the inductance associated with a tunable capacitor is just about as difficult. This inductance, together with the tunable capacitor, will resonate at a frequency known as the electrical self-resonance. For a frequency beyond the self-resonance, the inductance dominates the total device impedance, and the tunable capacitor then behaves inductively. Therefore, this associated inductance needs to be kept low enough so that the electrical self-resonance is much higher than the signal frequencies for which the tunable capacitor is designed. For example, let us assume a 10 pF capacitor will be used for signal frequencies up to 400 MHz. Therefore, the self-resonance of this 10 pF capacitor needs to be much higher than 400 MHz. Let us further assume that a factor of five greater than the signal frequency is needed, or a self-resonance of 2 GHz is adequate for the circuit design, the associated inductance, L, must then be less than $1/(\omega^2 C)$, or for our example less than 0.63 nH. The last and perhaps the most challenging parameter for a tunable capacitor is its linearity in response to RF power. Most applications require a tunable capacitor to have an extremely high linearity or to maintain an extremely constant capacitance value at any given tuned position in response to RF signal power. A third-order intermodulation product, or IP3, of greater than +50 dBm is often required. However, solid-state varactors have an inherent capacitance dependence on the signal power. Multiple varactor devices are often used in a parallel–series configuration, as shown in figure 21, to increase the overall linearity. This parallel–series configuration divides the total power by the number of series stages so that each individual varactor is required to sustain a much lower power level. The reduced total capacitance due to the series configuration of varactors can be 'made-up' by staging multiple varactor series in parallel. When the number of stages in parallel equals that in series, the overall parallel–series configuration, now much more linear as a whole, behaves similar to one single varactor in terms of capacitance tuning. The apparent drawback in this 'trick' is its use of an increased number of components, which can raise issues in reliability, cost, size, weight and power consumption.

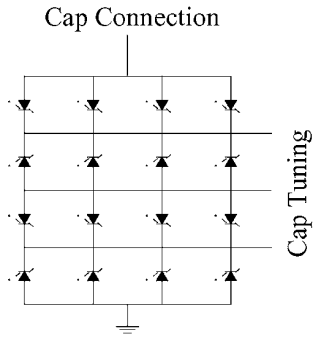

Figure 21. A parallel–series configuration to increase the over linearity of varactor diodes.

In summary, solid-state components, such as p–n junctions or Schottky varactors [52], have room for improvements in all these figures-of-merit categories. They often suffer from a small tuning ratio (typically 30% or less), excessive resistive loss caused by large series resistance and, thus, a low Q (typically in the low 10s), and a low electrical self-resonance, due to large parasitism especially when made on silicon substrates. Drastic measures are often required for the solid-state components to improve on one single parameter, for example, using light power to increase the tuning ratio [53].

Recent efforts within the MEMS field [54–64] have shown promising results in the realization of a MEMS-based high performance tunable capacitor. These MEMS tunable capacitors tune their capacitance by adjusting device physical dimensions via electromechanical means; the dielectric layer used is typically air, which eliminates the majority of the dielectric loss. Neglecting fringing effects, a capacitor with two electrodes of an area, A, separated by a gap, g, has a capacitance, C, where

$$C = \frac{\varepsilon A}{g} \tag{2}$$

and ε is the dielectric constant of the medium in the gap. There are two physical dimensional parameters (A and g) that can be varied, thus, the MEMS tunable capacitors can be classified into two categories based on their tuning schemes—gap tuning and area tuning, referring to the two capacitor dimensional parameters that are being altered to achieve the tuning functionality. The same set of figures of merit should be used in evaluating these MEMS tunable capacitors.

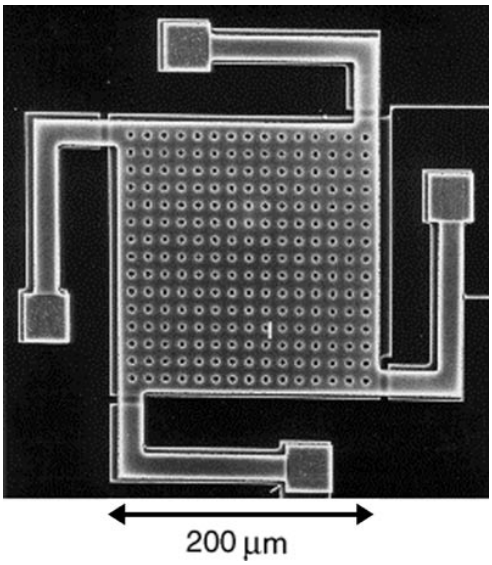

Figure 22. A top-view image of the University of California at Berkeley gap-tuning aluminium surface micromachined variable capacitor (from [55], University of California at Berkeley).

3.1. Gap-tuning capacitors

In 1996, Young and Boser published a gap-tuning capacitor using a surface micromachining technique [55]. One electrode is stationary on top of the substrate, and the other electrode of the tunable capacitor, supported by micromachined springs, is suspended over the stationary electrode and is movable in the vertical direction normal to the substrate. The gap between the movable and stationary electrodes can be electrostatically adjusted by applying a tuning voltage between the electrodes, resulting in a change in the device capacitance. Figure 22 shows a top-view image of such a device. Figure 23 shows an abbreviated cross sectional schematic illustration of the process sequence, details of which are described in [55]. The entire structure is made on top of a silicon wafer with an aluminium ground plane shielding the parasitics from the lossy silicon substrate to ensure a high Q. An oxide layer 4 μm thick is then deposited on top of the aluminium ground plane before the tunable capacitor is fabricated. This thick dielectric layer provides isolation between the device and ground, and maintains a parasitic capacitance below 220 fF. Aluminium (1 μm thick), used for both the bottom stationary electrode and the top movable electrode, is selected for its low sheet resistance, which is a prerequisite in minimizing resistive losses and achieving a high Q. The nominal electrode size is 200 μm by 200 μm, with an as-fabricated initial gap of 1.5 μm between the two electrodes. The capacitance varies from 2.11 pF with a 0 V tuning voltage to 2.46 pF with a 5.5 V tuning voltage, which corresponds to a tuning range of 16%. The equivalent series resistance is 1.2 Ω at 1 GHz, corresponding to a Q of 62. These measured performance parameters have matched or exceeded those of a state-of-the-art solid-state varactor.

The electrostatic actuation scheme is a preferred choice of tuning for its low power consumption. However, when electrostatic actuation is applied to a parallel plate system, the equilibrium between the electrostatic attracting force and the spring back force of the compliant supports holds only for a deflection smaller than, or equal to, one-third of the initial gap between the two parallel plates. Figure 24 illustrates a simple suspended beam system to demonstrate this effect. The spring back force, F_s, is

$$F_s = -k(d_0 - y) \tag{3}$$

where k is the spring constant and d_0 is the initial gap. The electrostatic force, F_e, is

$$F_e = \tfrac{1}{2}\varepsilon A V^2/y^2 \tag{4}$$

where V is the applied voltage. When one equates the two force terms, and solves the equation for the deflection y as a function of the applied voltage V, a critical solution can be found at a certain applied critical voltage, V_c, where y equals one-third of d_0. Mathematical details can be found in various textbooks or reference papers, such as [65]. Once this limit of one-third of the initial gap is surpassed, the electrostatic force, F_e, becomes larger than the spring back force F_s, and the suspended beam will snap down to, and be supported by, the bottom electrode in figure 24. Alternatively, one can use this bistable system to produce a switched-capacitor device by introducing a non-conductive dielectric film within the air gap such that the two electrodes

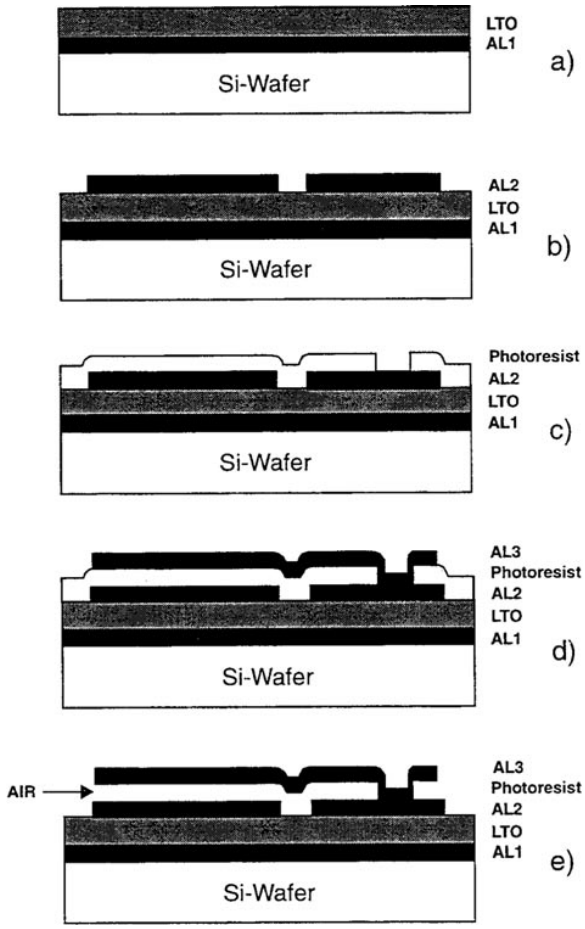

Figure 23. Cross sectional illustration of the process sequence for making a gap-tuning surface micromachined tunable capacitor (from [55], University of California at Berkeley).

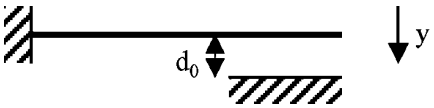

Figure 24. A schematic illustration of a simple suspended beam system.

do not short after the snap-down. Goldsmith *et al* [63] published a similar device using bistable MEMS membrane capacitor in 1999. By properly designing the device and the thickness of the dielectric film, a high tuning ratio of 22:1 was achieved between the two stable states of the membrane capacitor. However, many applications require continuous tuning of capacitance, as opposed to bistable switching between two capacitance states. This requirement limits the device operation to within one-third of the initial gap, and imposes a theoretical limit of 50% on the capacitance tuning range of any electrostatically actuated two-plate parallel plate system, because the maximum tuning range (MTR) is

$$\mathrm{MTR} := \left(\frac{\varepsilon A}{(1-\frac{1}{3})x_0} - \frac{\varepsilon A}{x_0}\right)\left(\frac{\varepsilon A}{x_0}\right)^{-1} = 50\%. \quad (5)$$

Dec and Suyama [58] proposed a three-plate parallel plate system in 1997 to increase this theoretical MTR limit from 50% to 100%. Figure 25 illustrates such a three-plate parallel plate system and figure 26 shows a top-view image of their tunable capacitor. The three-plate parallel plate system has two fixed plates; one suspended over the other. A third movable plate is made in between the two fixed plates, with air gaps on its two sides. The signal capacitor is between the topmost fixed plate and the movable plate ($C1$), while a separate tuning voltage can be applied to both $C1$, which is between the topmost plate and movable plate ($V1$), and $C2$, which is between the movable plate and the bottom fixed plate ($V2$). Therefore, the application of $V1$ will increase the capacitance of the signal capacitor $C1$, and that of $V2$ will decrease $C1$. The MTR of $C1$ with respect to $V1$, as well as that of $C2$ with respect to $V2$, still remain at 50%. However, the application of $V2$ also reduces $C1$ by approximately 50%, and the combination of $V1$ and $V2$ theoretically results in a total MTR of 100% for $C1$. The device is constructed using a multi-user MEMS polysilicon process (MUMPs) [66] available at MCNC. Polysilicon with a sheet resistance of $\sim 10\ \Omega\ \square^{-1}$ is used in this case for the superior mechanical properties needed in this more complex structure. The capacitor plates are 426 μm by 426 μm, with air gaps on the order of 0.75 μm. The capacitance of the signal capacitor $C1$ varied from 3.5 pF with $V1 = 0$ V and $V2 = 1.8$ V to 4.39 pF with $V1 = 0.7$ V and $V2 = 0$ V, corresponding to a tuning range of 25%. The device's Q is measured to be between 9.6 and 13.2 at 1 GHz.

In 1999, Feng *et al* [64] published a two-plate parallel plate tunable capacitor using an electro-thermal actuator instead of the electrostatic actuator. Figure 27 shows a top-view image of their tunable capacitor. The device is also made using the MCNC's polysilicon MUMPs process [66], and then flip-chip assembled onto an alumina substrate similar to [67]. The silicon substrate is then removed to improve the device's RF performance. The capacitance

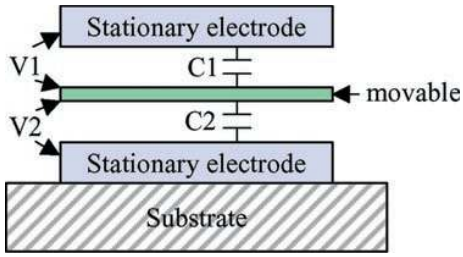

Figure 25. A three-plate parallel plate system with a movable electrode in between two stationary electrodes to increase the maximum tuning range to 100%.

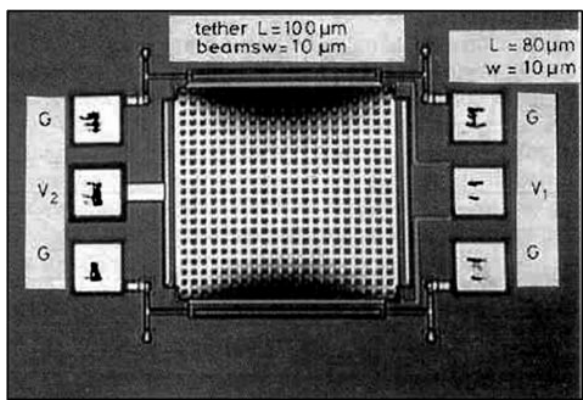

Figure 26. A top-view image of the three-plate gap-tuning variable capacitor developed by Dec and Suyama (from [58], Columbia University).

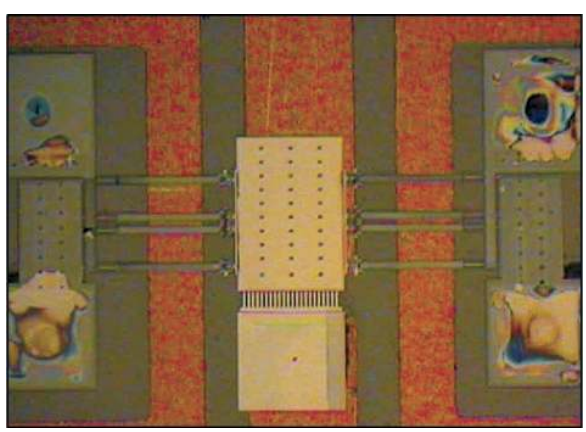

Figure 27. A top-view image of the University of Colorado gap-tuning variable capacitor using an electro-thermal actuator (from [64], University of Colorado).

value, measured at 13 MHz, can be tuned from an initial value of $\sim$0.9 pF to $\sim$1.7 pF at a tuning voltage of 5 V, corresponding to an almost 2:1 tuning ratio or about a 100% increase in capacitance. The extracted serial parameters for a typical device are $L = 0.262$ nH, $C = 0.102$ pF, and $R = 6.2\ \Omega$. The parasitic capacitance on the order of 0.5–0.6 pF is excluded in the serial-parameters extraction. The Q factor is 256 at 1 GHz for the 0.102 pF capacitance and the self-resonance is about 31 GHz. The use of an electro–thermal actuator is an attractive approach as it removes the theoretical tuning limit in an electrostatic actuator. However, the electro–thermal actuator consumes a certain amount of tuning

power and more than an electrostatic actuator does; typical values are 10 mA at 3 V.

The gap-tuning capacitors can be constructed using parallel plates stacked on top of a substrate using surface micromachining techniques. This approach provides an easy means to integrate the tunable capacitors with other conventional IC electronics. However, the theoretical 50% tuning range limitation in a basic design of a two-plate gap-tuning capacitor, or even the 100% limit in the three-plate design, falls short for some RF applications. Multiple numbers of tunable capacitors can be used in conjunction to increase the total tuning range, but the payoff is in its switching requirement and increased complexity, which often results disadvantageously in cost, reliability, and power consumption. Another inherent characteristic in a gap-tuning capacitor is the dependence of the device's RF power handling capability on the gap spacing between the two electrodes. As the capacitor is tuned higher in capacitance, the gap is reduced; RF breakdown in the capacitor air gap is thus more likely to occur. This aspect of the device must be taken into consideration when designing and using the device.

3.2. Area-tuning capacitors

Larson *et al* [54] first published in 1991 a MEMS area-tuning capacitor based on interdigitated comb structures. An electrostatic sliding micromotor is used to actuate a three-finger comb structure, and to change the overlapping area between the capacitor finger electrodes. The initiation voltage for this sliding micromotor is fairly high in the range 80—200 V because of the small fringing capacitance between the stator and rotor, and the high static coefficient of friction partly due to high electrostatic charge at the semiconductor surface. As a result, the structure was moved mechanically, as opposed to by an electrostatic means, to demonstrate the overlapping area change and the capacitance tuning. A capacitance value change from 35 fF to 100 fF was observed for a finger overlapping distance change from 150 μm to 375 μm, respectively. Further study is required to obtain electromechanical motion and capacitance tuning functionality.

Yao *et al* [60] (at the RSC) in 1998 published a MEMS area-tuning capacitor based on *suspended*, massively parallel, interdigitated comb structures fabricated using a deep reactive ion etch (DRIE) of single-crystal silicon which is later coated with metal thin film. One set of the comb structures is stationary and the other movable. When a tuning voltage is applied across the interdigitated comb structures, the electrostatic force at the fringes of the comb fingers laterally actuates the movable portion of the device, resulting in a change in the overlapping area of the capacitor structure, while the gap between the finger electrodes remains unchanged. Unlike the gap-tuning parallel plate system, there is no theoretical tuning limit for an area-tuning interdigitated comb structure. The only practical limits for the tuning range are within the supporting spring design and the length of the comb fingers. As long as the comb fingers are long enough for the structure to move, and as long as the deflection of the supporting spring is within the elastic region of the spring material, the capacitor device can be tuned. The electrostatic force is constant to first order with respect to the overlapping area.

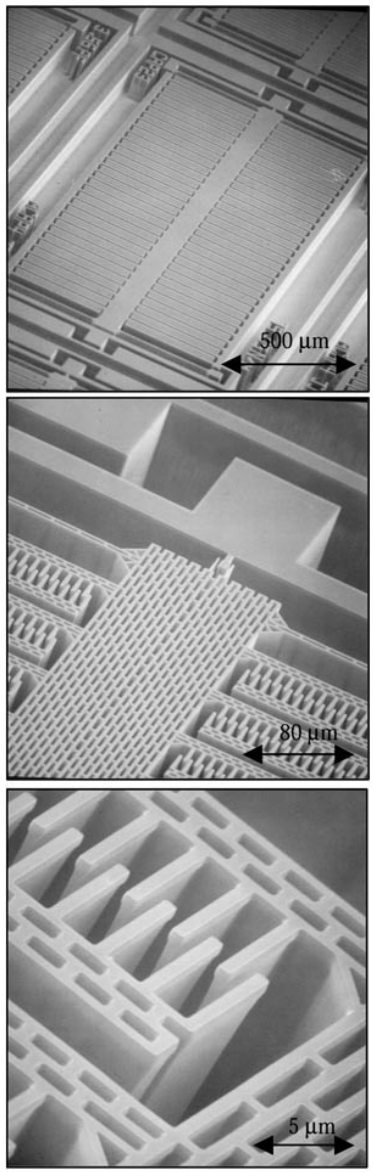

Figure 28. SEM images of the RSC area-tuning tunable capacitor at three different magnifications (from [60], RSC).

The objective for the first demonstration in the RSC tunable capacitor project is to show a MEMS silicon-based tunable capacitor having a continuous tuning range of at least 200%, or a 3:1 tuning ratio. Here, the tuning percentage is defined as the maximum tuned capacitance minus the minimum tuned capacitance and then divided by the minimum tuned capacitance, while the tuning ratio is defined as the maximum tuned capacitance over the minimum tuned capacitance. A secondary goal is to maintain fair device integrity for other parametric requirements of the tunable capacitor, including a high Q factor or a minimum equivalent series resistance, a high electrical self-resonant frequency or a small inductance value, and a good linearity in response to RF signal power. Figure 28 shows three SEM images at different magnifications of a RSC tunable

capacitor. The tunable capacitor typically occupies an area of 1 mm^2, and is comprised of a large array of interdigitated comb fingers, which are nominally 2 μm in width, 2 μm spaced, and 20–30 μm in height. The supporting springs are typically 1 mm in length, and have the same width and height as the comb fingers. Figure 29 illustrates an abbreviated schematic process flow for such a silicon-based area-tuning capacitor. The details of the fabrication process are described in [60]. The starting material is a silicon-on-insulator (SOI) wafer, with the device silicon layer approximately 20–30 μm thick and a silicon dioxide interlayer of about 0.5–2 μm. The structural pattern of the tunable capacitor design is first transferred to the device single-crystal silicon layer using photolithography and a SF_6-based inductively coupled plasma (ICP), which gives an anisotropic deep silicon etch, stopping on the underlying silicon dioxide layer. Figure 30 is a SEM image of a cross sectional view of the silicon lines and spacing created using this technique. The nominal dimensions are those described above. The back side of the silicon wafer is then photolithographically patterned, with alignment to the front-side structure. A second ICP deep silicon etch is performed to remove the portion of the silicon substrate directly underneath the interdigitated comb structure. This selective silicon substrate removal step minimizes parasitic losses from the lossy silicon substrate. The buried silicon dioxide layer is then selectively removed using hydrofluoric acid, and dried in a super critical carbon dioxide vessel. A coat of aluminium is sputtered on after the structural release from both the front and back sides of the wafer to reduce the equivalent series resistance of the tunable capacitor device. During the metal sputtering, the suspended structure naturally creates an electrical discontinuity between the electrodes within the capacitor and between the capacitor and the substrate. No further metal lithography or etching steps are needed. This results in a two-mask MEMS process that provides a low-parasitic structure, electrical isolation and interconnect metallization. It should be noted that a low-resistivity (e.g., 10–20 Ω cm) silicon substrate has been found quite lossy and contributes significantly to the total parasitic capacitance in the bond pad areas. Parasitic capacitance as high as 2 pF for such a silicon substrate has been observed in a tunable capacitor with a nominal capacitance of 3 pF. For the same device, the 2 pF parasitic capacitance is reduced to 0.2 pF when a high-resistivity (e.g., $>$4000 Ω cm) silicon substrate is used. Figures 31(a) and (b) show the RF characterizations of these parasitic effects in the form of S11 parameters [50]. These high-resistivity silicon substrates are now readily available [68] as float-zone technology advances.

Alternatively, an insulating substrate, such as a glass substrate, can be used to replace the silicon substrate. This can further reduce the parasitic effect as glass substrates are more resistive and less lossy than silicon substrates. For the same device as in the example above, the parasitic capacitance, as shown in figure 31(c), is reduced to 0.08 pF when a glass substrate is used [50]. Figure 32 schematically illustrates a process flow to make a tunable capacitor on a glass substrate, and figure 33 shows a top-view image of such a device. A silicon wafer consists of a silicon substrate, an etch-stop layer, and a single-crystal silicon device layer

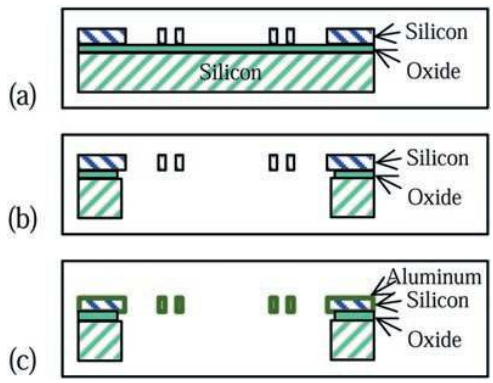

Figure 29. Schematic cross sectional illustration of the process sequence for making a RSC MEMS tunable capacitor based on SOI wafer structures (from [60], RSC).

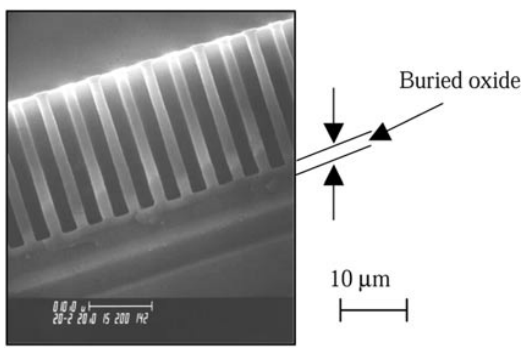

Figure 30. SEM image showing 20 μm deep silicon lines spaced 2 μm apart on top of a buried oxide film. The structure is created using ICP DRIE (from [60], RSC).

adhesively bonded to a glass substrate. The silicon substrate material is then removed using a grinding and polishing step followed by a chemical etch in tetramethylammonium hydroxide (TMAH), stopping on the underlying stop layer, which is later removed as well. This results in a material structure consisting of a single-crystal silicon device layer, an adhesive layer, and the glass substrate. In the RSC tunable capacitor device, the silicon layer is between 20 and 30 μm thick, and the adhesive layer is nominally 20 μm thick. The structural pattern is then defined in the device silicon layer using photolithography and the SF_6-based ICP process (figure 32(a)). The adhesive layer is selectively removed in an oxygen plasma to release the tunable capacitor while the large bond pads and anchoring areas remain attached to the glass substrate (figure 32(b)). A coat of aluminium is sputtered on after the structural release to reduce the equivalent series resistance (figure 32(c)). As in the fabrication of the SOI-based tunable capacitor above, the suspended structure, during the metal sputtering, naturally creates an electrical discontinuity between the electrodes within the capacitor and between the capacitor and the substrate. The entire process uses a single masking step.

The tunable capacitor on glass substrate, as shown in figure 33, is configured with the central movable structure electrically grounded. There are two sets of fixed electrodes on the side. In conjunction with the central movable structure, these two sets of fixed electrodes form two tunable capacitors

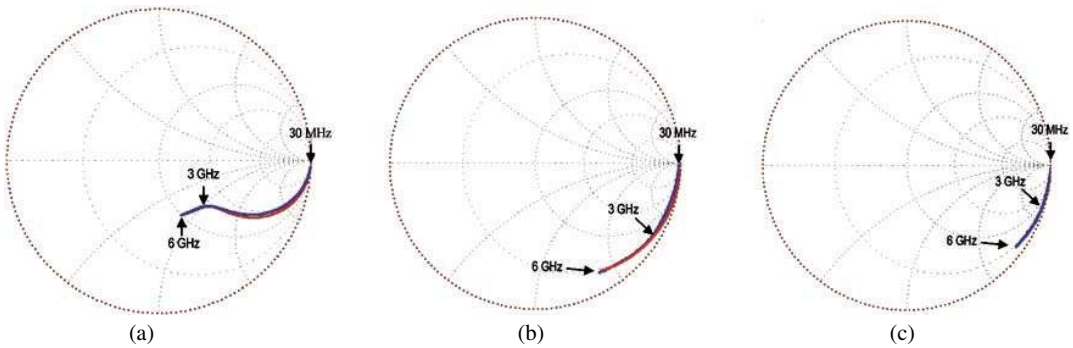

Figure 31. S11 plots in Smith charts of parasitic capacitance when the tunable capacitor is made on (a) low-resistivity silicon substrates, 2.05 pF; (b) high-resistivity silicon substrates, 0.212 pF; and (c) glass substrates 0.0825 pF (from [48], RSC).

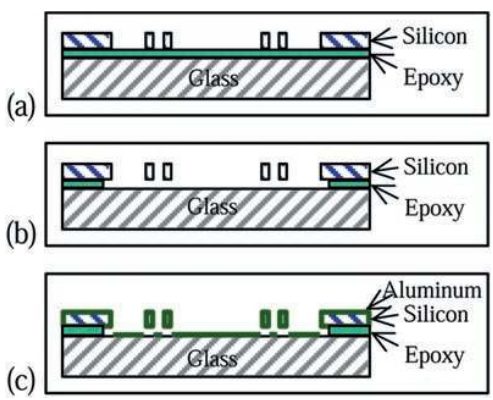

Figure 32. Schematic cross sectional illustration of the process sequence for making a RSC MEMS tunable capacitor on glass wafer substrates (from [50], RSC).

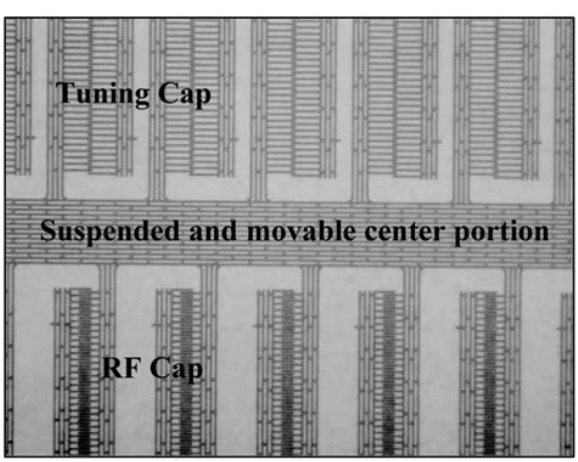

Figure 33. A micrograph image of a RSC MEMS tunable capacitor with two mechanically joined tunable capacitors—one for tuning and the other for the RF signal. The central movable portion is electrically grounded.

that are mechanically joined together—one for tuning and the other for RF signals. This configuration is preferred whenever applications have one terminal of the RF capacitor grounded, because biasing inductors, or RF chokes, can be eliminated when the tuning mechanism is electrically isolated from the RF path, as illustrated in figure 34. Figure 35 shows a S11 plot in a Smith chart of a RSC tunable capacitor on a glass substrate, with a capacitance of 5.19 pF. The electrical

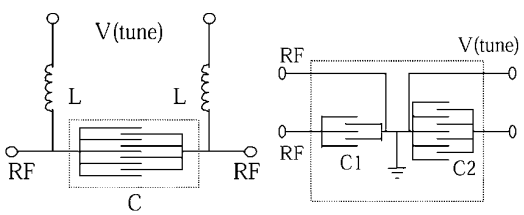

Figure 34. Schematic illustrations of MEMS tunable capacitors. The dashed boxes highlight the MEMS portion.

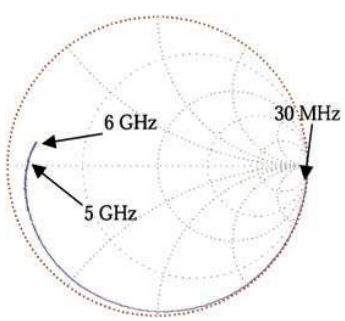

Figure 35. S11 plot of a RSC MEMS tunable capacitor in a Smith chart showing a self-resonance of 5 GHz.

self-resonance of this capacitor is 5 GHz, corresponding to an inductance of approximately 0.19 nH. At 500 MHz, where the tunable capacitor will be used, the equivalent series resistance is 1.8 Ω, corresponding to a Q of 34. Figure 36 contains a series of images showing a portion of the tunable capacitor at tuning voltages of 0, 2, 4, and 5 V. The change in the overlapping area of the interdigitated comb fingers indicates a change in capacitance, which is plotted graphically in figure 37(a). The total capacitance including all parasitic effects is measured as 5.19 pF at 0 V and 2.48 pF with a tuning voltage of 5 V. This corresponds to a tuning range of about 100%. This reversed capacitance tuning with an increasing tuning voltage lowering the RF capacitance mimics the behaviour of varactor diodes, and thus minimizes the number of changes required in the capacitor drive circuitry for MEMS insertion. Alternative proportional capacitance tuning has also been demonstrated, as shown in figure 37(b), with a tuning range of 200% at a tuning voltage of 14 V. The linearity of the tunable capacitor is still under investigation, although preliminary results have indicated an IP3 of greater than +50 dBm.

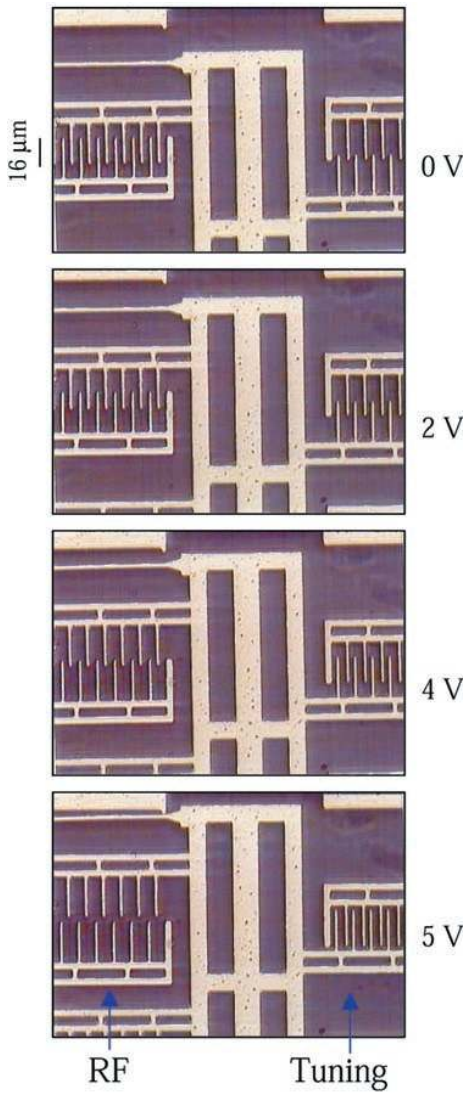

Figure 36. A series of images showing a portion of the RSC MEMS tunable capacitor with a tuning voltage of 0–5 V.

The area-tuning capacitors have shown promising results in all figures of merit listed earlier. Furthermore, the interdigitated comb structure based tunable capacitors do not have any theoretical tuning range limitation, as do the parallel plate based gap-tuning capacitors. The RF power handling capability of an area-tuning capacitor is independent of the tuned capacitance because the gap between the comb electrodes remains constant. However, the process required to make such a tunable capacitor remains a challenge for integration with other electronic ICs. With further work, and some of it is already ongoing, the full integration of these tunable capacitors with electronics is considered possible. The size of the device is still quite large because the total capacitance per unit area for such a comb structure based capacitor heavily depends on the aspect ratio of the comb fingers. With the present ICP technology, an aspect ratio of 20:1 is about the best achievable for a minimum critical dimension of 2 μm.

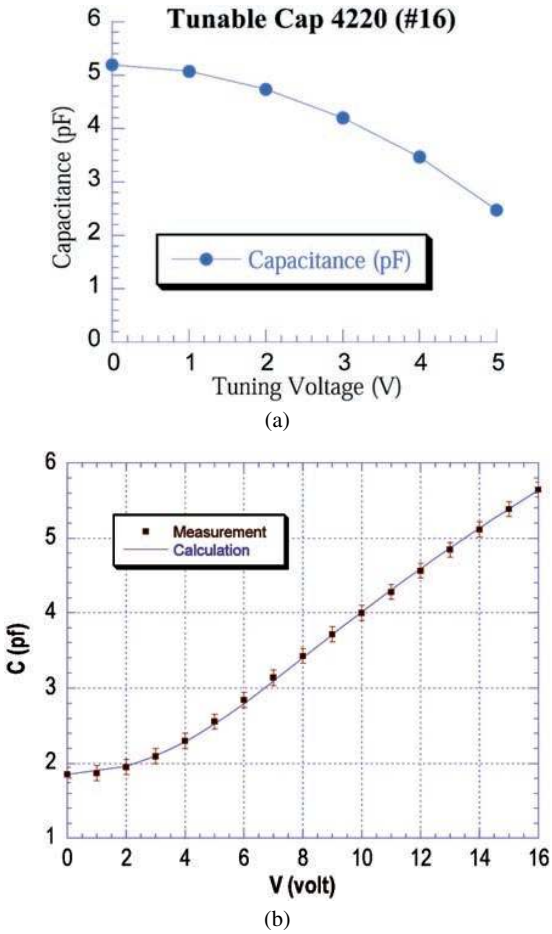

Figure 37. (a) Capacitance plotted as a function of the tuning voltage for the device shown in figure 36, and (b) proportional capacitance tuning has also been demonstrated with a 200% tuning range at 14 V.

3.3. Characteristics and performances of tunable capacitors

Similar to the RF switch case, device parameters for a tunable capacitor have various levels of importance in various applications, and often with conflicting requirements. Tradeoffs among them and the final device selection are also heavily guided by the targeted applications. The challenging task of device comparison for general RF applications is consequently replaced by enlisting representative characteristics and device performance parameters of a selected number of MEMS tunable capacitors, as tabulated in table 2. Solid-state varactor diodes are used as the baseline device. MEMS tunable capacitors listed in table 2 include devices by the University of California at Berkeley (figure 22) [55–57], Columbia University (figure 26) [58, 59], University of Colorado (figure 27) [64], HRL Labs [54], and the RSC (figures 28 and 33) [50, 60]. It should be noted that, due to space limitation, some of the MEMS tunable capacitors are not listed here, and they should by no means be considered inferior because of their absence.

A varactor diode has a capacitance value inversely proportional to the tuning voltage. The minimum capacitance is thus at the highest tuning voltage, and the capacitance increases as the tuning voltage decreases. In our example

Table 2. Characteristics and performances of selected MEMS tunable capacitors. Note, for the varactor diodes average solid-state varactors are used for comparison.

Device characteristics and performance parameters	Varactor diodes	University of California at Berkeley [55–57]	Columbia University [58]
MEMS technology	—	Surface	Surface
Device size (μm × μm)	Discrete SC-79	∼800 × 800	∼450 × 450
Structural material	Silicon	Aluminium	Polysilicon
Actuation mechanism	Hyperabrupt junction	Electrostatic	Electrostatic
Actuation voltage (V)	4	5.5	1.8
Minimum capacitance (pf)	2 at 4 V	2.11	3.5
Tuning range (%)	335	16	25
Tuning range limit (%)	—	50	100
Series resistance (Ω)	2.8	1.2 at 1 GHz	—
Quality factor, Q	350 at 50 MHz	62 at 1 GHz	9.6 at 1 GHz
Series inductance (nH)	1.5	Not available	Not available
Self-resonance (GHz)	∼1.3	>1.2 GHz[d]	>5 GHz[d]
Linearity	Poor	Not available	Not available
Others	Data obtained at packaged level (surface mount)	Data obtained for four tunable caps in parallel	Data obtained at proble level with bond pads included

Device characteristics and performance parameters	University of Colorado [64]	HRL[a] [54]	Rockwell RSC [48, 60]
MEMS technology	Surface + Bonded	Surface	Bonded wafer
Device size (μm × μm)	∼500 × 800	∼150 × 500	∼1000 × 2000
Structural material	Polysilicon	Au	Silicon
Actuation mechanism	Electro-thermal	Sliding motor	Electrostatic
Actuation voltage (V)	5	80–200[b]	2–14
Minimum capacitance (pf)	0.9	0.035	1.8
Tuning range (%)	∼90	185	200
Tuning range limit (%)	—	—	—
Series resistance (Ω)	6.2[c]	Not available	1.8
Quality factor, Q	256 at 1 GHz[c]	—	34 for 5.19 pF at 500 MHz
Series inductance (nH)	0.262[c]	Not available	0.19
Self-resonance (GHz)	31[c]	—	5 for 5.19 pF
Linearity	Not available	Not available	IP3 > +50 dB m
Others	The electro-thermal actuator draws a current of about 10 mA	Cap change was measured using mechanical motion	Tuning is electrically isolated from RF. Requires no chokes.

[a] Possible work after 1991 [54] is not available.
[b] 80–200 V to initiate movement of the structure.
[c] Values extracted from S-parameters for $C = 0.102$ pf. Bond pads and parasitics are excluded.
[d] Representing the highest frequency measured.

varactor diode in table 2, the minimum capacitance is 2 pF when a maximum tuning voltage of 4 V is applied. For all the MEMS tunable capacitors in table 2, with the exception of a version of the RSC devices, the capacitance value increases proportionally with the tuning voltage.

For a tunable capacitor device that can be modelled as an ideal capacitor with a pure resistor and inductor in a serial configuration, the quality factor Q has an inversely proportional relationship with the series resistance, as does the electrical self-resonance with the serial inductance. However, parasitics often play a major role in the total device impedance, and the tunable capacitor device may not be modelled as a simple serial connection of a resistor, an inductor, and a capacitor. Consequently, an attempt is made to list all four parameters in table 2. It should also be kept in mind that, in addition to its dependent relationship with equivalent series resistance, Q is also a function of the frequency and the capacitance. A similar interdependent relationship is true for the self-resonance frequency with the inductance and the capacitance. Therefore, these two parameters should be compared among devices only when the frequency and capacitance values are scaled to the same level.

Along with its integration capability, linearity with respect to input RF power is perhaps one of the most important criteria for a MEMS tunable capacitor. The lack of linearity is a major shortcoming for a solid-state varactor, and is inherent within the solid-state device. Hence, much of an improvement in linearity for a varactor diode is not highly promising, which then becomes a significant motivation for the development of MEMS-based tunable capacitors. However, few data are available at this point.

4. High-Q inductors

High-performance integrated inductors are in increasingly higher demand in modern communications products. Applications include filters, oscillators, low-power converters, and various applications in RF front ends of wireless transceivers. Key parameters in integrated inductors are the quality factor Q and the self-resonance frequency where Q would peak

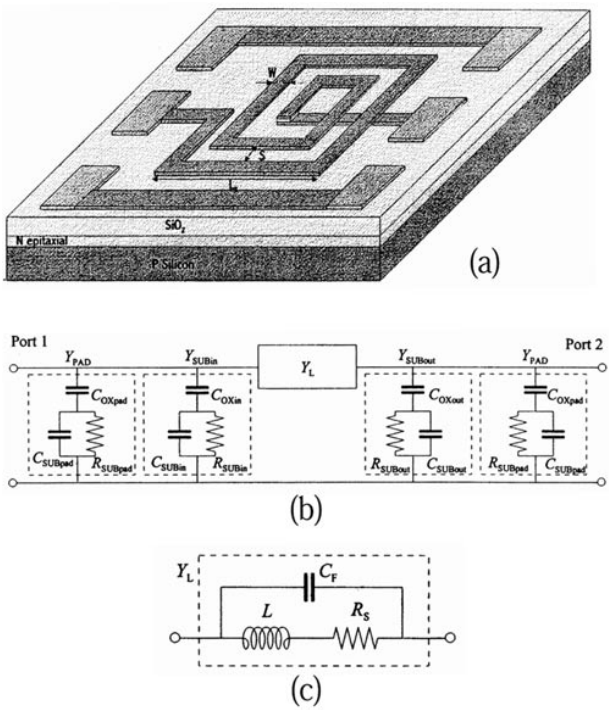

Figure 38. (a) A typical integrated spiral inductor with (b) an equivalent circuit showing various parasitic elements and (c) a model of the inductor device (from [70]).

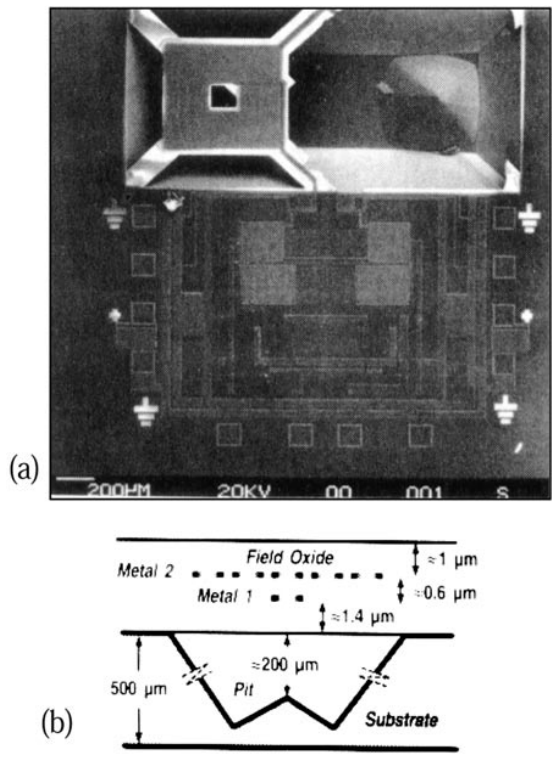

Figure 39. (a) SEM image and (b) schematic cross sectional illustration of a spiral inductor suspended on a CMOS silicon substrate (from [71], UCLA).

as the device transforms from inductive to capacitive characteristics. Resistive metal lines and dielectric losses in the substrate are the main contributing factors to the degradation of the Q factor, while various fringing and parasitic capacitances limit the self-resonance of an inductor. Significant efforts have been emphasized in the analysis and modelling of integrated spiral inductors in the search for a better understanding of the device and, more importantly, for a solution to the challenging problems [69, 70]. The resistive nature of thin-film metal technology, dielectric loss in a CMOS silicon substrate, and the close coupling between spiral turns are all significant barriers for integrated on-chip inductors. Figure 38 shows a typical spiral inductor on a silicon substrate with major parasitic elements identified in the schematic diagram [70]. Efforts were focused on dimensional and material optimizations to minimize the associated resistance and capacitance. Metals such as Cu and AlCu were investigated. However, Qs greater than 10 at a frequency beyond 2 GHz remain challenging for conventional IC technologies.

In addition to the integration incompatibility, discrete inductors also suffer from RF gain losses due to the large parasitic capacitance of the bond pad, bond wires, packaging leads, and board traces. These losses make the discrete parts even less desirable and urge for an integrated solution. In 1993, Abidi's research group at UCLA presented a paper, Chang *et al* [71], where a spiral inductor was made on a 2 μm CMOS silicon wafer with the portion of silicon substrate directly underneath the inductor removed to minimize the substrate parasitic effect. Figure 39 shows an image of their suspended spiral inductor [71]. A 20-turn aluminium square spiral inductor with a 4 μm line width and spacing, and an outer dimension of 440 μm was made that resulted in an inductance of 127 nH. The silicon substrate was then etched using a liquid-phase anisotropic etchant, creating an air cavity 200 μm deep directly below the inductor. No lithography or additional masking steps were needed for this cavity formation. As a result, the self-resonance increased from 800 MHz before the silicon etch to 3 GHz after, and the relative quality factor (L/R) increased to 127 nH/160 Ω, equivalent to a Q of approximately 5 at 1 GHz, which is fairly high for the inductance and frequency. Later in 1996, the same research group published [72] a gas-phase based isotropic etching method of the silicon substrate that resulted in a smaller footage for the cavity, but with similar self-resonance improvement and Q for the inductor.

UCLA's method of substrate micromachining essentially created a membrane platform for the inductor so that the parasitic capacitance between the device and the silicon substrate is minimized. This method can also be applied to other RF components to minimize parasitic effects, especially for silicon-based RF ICs. Other platforms for minimizing parasitic effects have since been demonstrated with promising results. Fan *et al* [73] demonstrated a platform using a surface-micromachined micro-elevator by a self-assembly (MESA) technique. The MESA platform was fabricated using the MCNC's polysilicon MUMPs process [66] and scratch drive actuator for the assembly. A 12.5-turn circular spiral inductor with an outer diameter of 137 μm was made on the platform, which resulted in a 24 nH inductor suspended 250 μm above the silicon substrate. The self-resonance of the inductor increased from 1.8 GHz, before the suspension, to 6.6 GHz after. Q values were not reported in the paper. Ziaie *et al* [74] demonstrated

another micromachined platform for RF applications. A Colpitts oscillator transmitter of 5 mm by 5 mm with a two-turn dielectric suspended inductor was manufactured on the platform, which consists of a dielectric membrane suspended over a glass substrate. A Q of 22 was measured at 275 MHz for the inductor with an inductance of 115 nH. The self-resonance of the inductor is greater than 750 MHz.

A high-energy magnetic core can be used to significantly increase the total inductance. Numerous research efforts have been devoted to this aspect of micromachined inductors in the past few years [75–78]. However, the relative permeability of the magnetic core material decreases significantly as the frequency increases beyond a certain critical value, depending on the core material. The plated Ni–Fe permalloy in [75], for example, decreases significantly in its permeability for frequencies higher than 3 MHz. In general, high-permeability materials for frequencies beyond 100 MHz are difficult to find. Therefore, the high-energy magnetic core approach to an inductor is more suitable for applications such as microactuators and power conversions, as the [75–78] originally intended, and is not well suited for RF applications.

MEMS technology also enables the manufacturing of devices and structures into the third dimension. These 3D structures have the advantages of being suspended and having very low parasitic capacitance. In 1999, Yoon *et al* [79] demonstrated a 3D spiral inductor using Cu metal lines on a glass substrate, as shown in figure 40 [79]. In this 3D fabrication method, plated Ni is used as the moulding material for Cu plating. A multiple-layered structure can thus be made, as shown in figure 40(b), with the sacrificial Ni mould removed at the end of the process. Inductors made on a glass substrate have shown a Q of 57 at 10 GHz with an inductance of 1.75 nH (figure 40(a)) and a Q of 38 at 1.8 GHz with an inductance of 14 nH (figure 40(b)). Further exploring 3D manufacturing with MEMS technology, Young *et al* [56, 57] demonstrated a 3D coil inductor with a low-loss alumina core. Figure 41 shows an image of such a device. Copper traces 5 μm in thickness were plated around the alumina core, which is approximately 500 μm in width and height. A Q of 16 was measured at 1 GHz for a two-turn inductor with an inductance of 8.2 nH.

These various MEMS-based inductor designs have shown an increased Q and self-resonance frequency over more conventional integrated spiral inductors. In the mean time, Zhou *et al* [80] at NJIT pursued a method to switch inductor networks by combining micromachined relays with spiral inductors. The relays are made of a $TaSi_2/SiO_2$ bimorph cantilever beam with combined thermal and electrostatic actuation. The inductors are made using a spiral design on a membrane with the portion of silicon substrate directly underneath the inductor area removed. A 4 bit switched inductor network has been demonstrated with a measured total inductance ranging from 2.5 to 324.8 nH. The self-resonance is 1.9 GHz with a Q factor of 1.7 at a frequency of 530 MHz for the switching configuration that produces 324.8 nH. For other switching configurations, the total inductance is lower, hence the self-resonance is higher.

Although the Q factor has room for improvement in this variable inductor network, the demonstration of a switched inductor bank or digitally tuned inductance that also can be

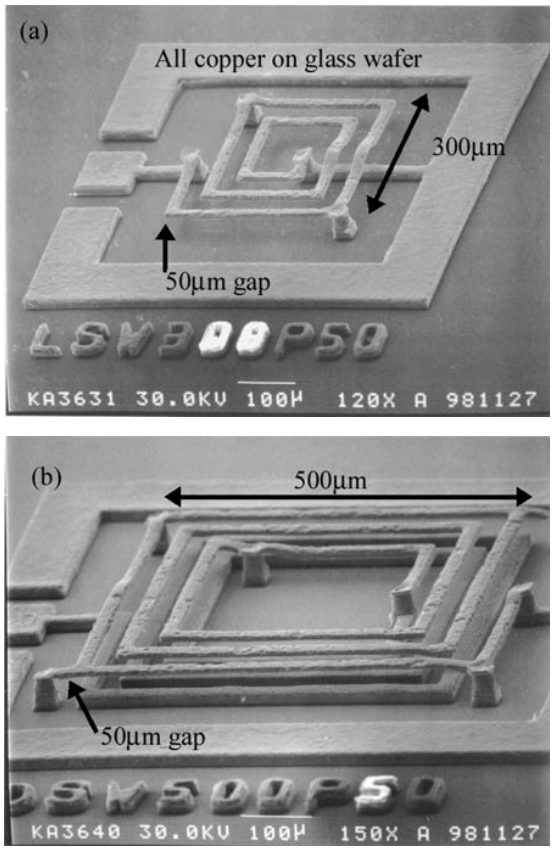

Figure 40. 3D Cu spiral inductors made on a glass substrate (from [79], KAIST).

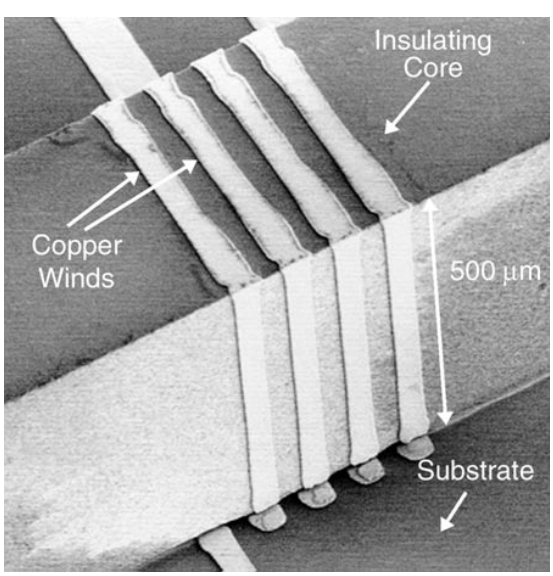

Figure 41. 3D Cu coil inductor with a low-loss alumina core (from [56], Berkeley).

monolithically integrated with other electronic ICs has many promising aspects. The combination of the tuning function in this work with some of the high-Q 3D inductor devices discussed earlier should bring tremendous advantageous benefits to the pursuit of a fully integrated radio on a chip or other advancements in RF applications. Packaging for these MEMS devices integrated with IC electronics, however,

remains challenging because of the substrate engineering and the 3D nature of the devices.

5. Application example—A two-pole filter using MEMS lumped elements

Device performance parameters of the RF passive and reactive elements have been continuously emphasized throughout the earlier sections on RF switches, tunable capacitors and integrated inductors. They must be considered the highest priority during design and development, simply because the performance of the products in which these components are used heavily depends on these device parameters. Details may differ from product to product and from device parameter to device parameter. However, there is a strong general dependent relationship between the products, be it an oscillator, tunable filter, VCO, or whatever circuit module, and the device parameters of the RF MEMS components that are used in those products. Under DARPA-MTO sponsorship, RSC, teamed with Rockwell Collins, is developing MEMS RF switches and MEMS tunable capacitors to be evaluated for future insertions into tracking filters for antenna interface units (AIU) in various military applications [50]. The targeted specifications used for the development of these MEMS components are those of the AIUs in F22 Air Superiority Fighter and RAH-66 Comanche helicopter. The detailed tracking filter designs in the DARPA-sponsored program are beyond the scope of this paper. However, a much simpler filter example using the MEMS components can help the readers to have a better understanding of the importance of the component performance parameters to the final products. The purpose of this section is to demonstrate this dependent and important relationship between the MEMS components and the final products in which the components are used.

As an example, a generic two-pole bandpass filter is discussed in this section. In this partial and incomplete design of the filter, the insertion loss is the *only* filter parameter being considered and the quality factor, Q, and the self-resonance frequency of the RF MEMS components are the *only* parameters being examined. Other parametric analysis should concur with the result of this example on the importance of the device parameters. Figure 42(a) shows a schematic diagram of a two-pole bandpass filter. Note that all the inductors in the filter can potentially be replaced by MEMS high-Q integrated inductors, and the variable capacitors by MEMS tunable capacitors or MEMS RF switches in series with fixed high-Q capacitors to provide a switched capacitance tuning function. This could eliminate the need for off-chip inductors and varactor diodes with poor linearity characteristics. With proper selection of the device values as listed in figure 42, the filter has a passband centred around 200 MHz, as shown in figure 43 (trace A). This assumes a set of near perfect parameters with a self-resonance frequency of 10 GHz and a Q factor of 5000 at the resonance frequency for all elements in the filter. However, in actuality, each capacitor has its associated serial inductance and resistance, as does each inductor as modelled in figure 42(b). Note that, for a capacitor, Q is defined as $1/(\mathrm{j}\omega C R_c)$ and the self-resonance frequency ω_r is $\sqrt{1/(CL_c)}$; and for an inductor, Q is defined as $\mathrm{j}\omega L/(R_L)$ and its self-resonance frequency ω_r is $\sqrt{1/(LC_L)}$. Hence, all the associated inductance, capacitance, and resistance can be expressed to first order in the terms of Q, ω_r, and either C or L.

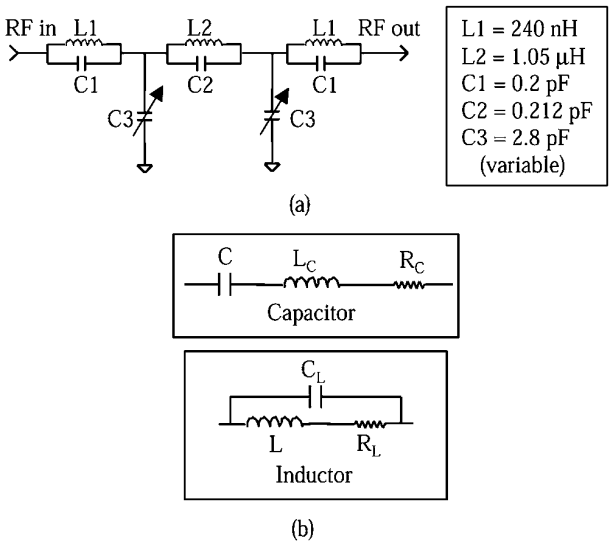

Figure 42. An example two-pole filter for demonstration of its dependence on MEMS device parameters with (a) a schematic diagram and (b) device models.

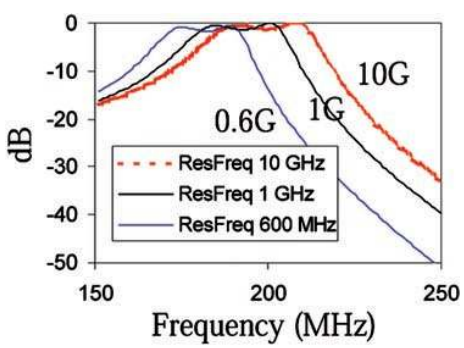

Figure 43. Filter responses showing their dependence on the self-resonance of the devices used.

Figure 43 shows three traces of the filter's frequency response, corresponding to three self-resonance frequencies of 10 GHz, 1 GHz, and 600 MHz for all the capacitors and inductors used in the filter. As the self-resonance frequencies become lower, the associated parasitic reactance and series resistance become more significant to the filter's characteristic response. The central frequency of the passband is pushed lower from the designed 200 MHz. At a self-resonance frequency of 600 MHz, the filter's passband is at 182 MHz, approximately 10% lower than the designed frequency. Should the self-resonance frequency further drop to about 200 MHz, which is equivalent to introducing unwanted zeros at 200 MHz, bandpass filters centring at that frequency can no longer be constructed.

Figure 44 shows three traces of the filter's frequency response with a Q of 500, 100, and 50 at 1 GHz for all the components used in the filter. The self-resonance frequency is assumed to be 1 GHz also. At a Q of 500, the insertion

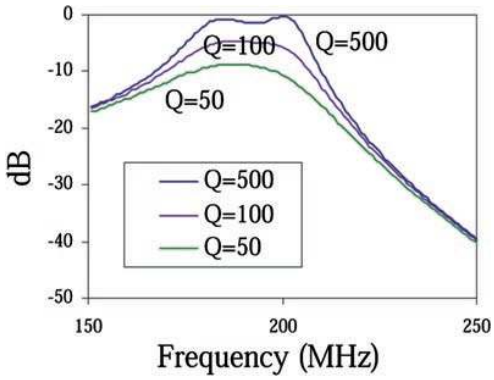

Figure 44. Filter responses showing its dependence on the Q factor of the devices used.

loss of the filter is minimal, but when Q is decreased to 100, the insertion loss is about 4.6 dB, or approximately 40% of the signal is lost when passing through the filter in its passing band. When the Q further decreases to 50, the insertion loss becomes 8.7 dB, and about 65% of the signal is lost. Therefore, the device parameters are extremely important to the performance of the final products in which the MEMS components are used. Other device parameters, such as isolation and linearity, can be shown of equal, if not more, importance using similar analyses.

6. Mechanical resonators and filters

At the same time as MEMS efforts continue to improve and optimize the device parameters of the RF switches, tunable capacitors, and integrated inductors, researchers focusing on high-Q filter applications, specifically, are investigating an alternative approach using mechanical resonators. These mechanical filters transform electrical signals into mechanical energy, perform a filtering function, and then transform the remaining mechanical energy back into an electrical form. Unlike other electromechanical filters such as quartz-crystal filters and ceramic filters that are composed of *electrically* coupled resonators, and SAW (surface acoustic wave) filters that have *uni-directional* signal propagation, a mechanical filter is an electromechanical filter that is composed of *mechanically* coupled multiple lumped mechanical resonators, and allows *bi-directional* signal propagation within the filter. Since the first development of mechanical filters in 1946 by Robert Adler of Zenith [81], a large world-wide effort has been focused on the mechanical filter optimization and the development of new-generation filters, leading quickly to the mass production of these mechanical filters in the 1950s for telephone applications. Figure 45 (from [82]) shows an actual mechanical filter with disk resonators coupled with mechanical wires, made by Rockwell International for use in FDM (frequency-division multiplex) telephone systems, and the equivalent circuit of this mechanical filter. The reason behind the rapid development and then adaptation of the mechanical filter is its superior characteristics, including a high Q, good temperature stability, and aging properties, which are all critical in achieving low-loss, narrow bandwidth, and high-stability filters.

The design of a mechanical filter involves basic principles of physics, electromechanical transducer concepts, vibration theories, and filter circuitry. Johnson wrote an excellent book in 1983 entitled *Mechanical Filters in Electronics* [82], which discusses in detail the design of mechanical filters. These early macroscopic mechanical filters, such as that shown in figure 45, have a typical central frequency below 600 kHz due to their size and manufacturing capability. The insertion losses are typically about 2 dB. However, in modern day communication applications, the central frequencies are much higher and much lower insertion losses are required. The traditional macroscopic mechanical filters are thus less applicable, although the concept and its inherent superior characteristics remain attractive.

As in many other examples, MEMS technology was applied to the miniaturization of mechanical resonators. The most representative design is a polysilicon interdigitated comb device with double-folded support structure published in 1989 [83]. A mechanical filter based on these resonators was first published in 1992 [84]. Since then, a number of papers have been published on the optimization of these mechanical filters [85–89], and on alternative MEMS-based resonator designs [90–93]. In general terms, a single resonator can be simplified to a spring–mass system with a resonance frequency, f_1, and

$$f_1 = \frac{1}{2\pi}\sqrt{\frac{k_1}{m}} \tag{6}$$

where k_1 is the stiffness of an ideal spring without mass and m is the resonating mass without compliance. When two identical spring–mass resonators are connected side by side with a third spring hinged between the two resonating masses, as shown in figure 46(a), there are two resonance frequencies for the system. The first resonance is when the two resonators are in phase, as shown in figure 46(b), where no energy is being stored in the coupling third spring. Therefore, the coupling spring can be removed without interfering with the overall system, and the resonance frequency is the same as that of a single-resonator system. The second resonance is when the two resonators are 180° out of phase, as shown in figure 46(c). Note that there is no displacement at the mid-point of the coupling spring. Therefore, the out-of-phase resonance can be modelled as a single resonator with two springs, as shown in figure 46(d), where the new spring has twice the stiffness of the coupling spring. The resonance frequency, f_2, is

$$f_2 = \frac{1}{2\pi}\sqrt{\frac{k_1 + 2k_2}{m}} \tag{7}$$

where k_2 is the stiffness of the coupling spring. This in-phase and out-of-phase resonance characteristic can be seen in higher-order coupled-resonator systems, with *all resonators in phase* being the lowest resonance, *all adjacent resonators* 180° *out of phase* being the highest resonance, and all other configurations in between. With proper design, these resonance frequencies can be moved in the frequency spectrum, and the overall system frequency response can be shaped to produce a desired bandpass filter. Figure 47 shows a MEMS-based mechanical filter with three resonators

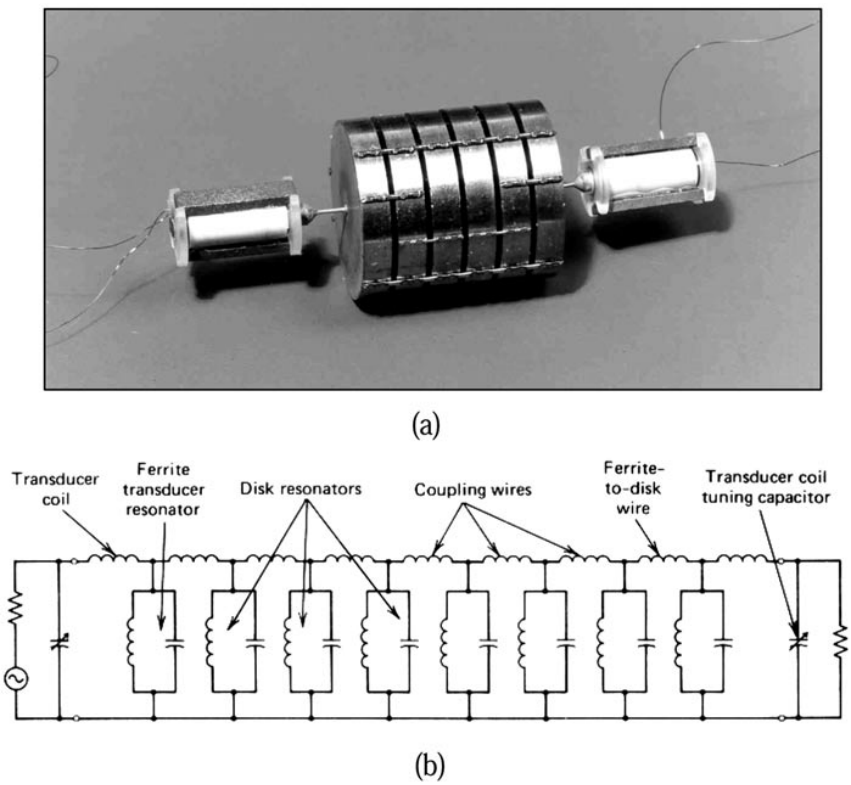

Figure 45. (a) A mechanical filter and (b) its equivalent circuit representation used in FDM telephone systems by Rockwell International (from [82], Rockwell).

mechanically coupled together [85]. The entire filter structure is made of doped polysilicon 2 μm thick and suspended 2 μm above a ground plane. Each of the resonators has a folded-beam design with a Q of approximately 25 000 at 40 mTorr pressure. The beam length is 32.8 μm and the width is 2 μm. The filter has a passband width of 510 Hz, centred at 300 kHz, and a Q of 590, an insertion loss of 3 dB, a stopband rejection of 38 dB, a 20 dB down shape factor of 1.45, and requires a dc bias of 150 V. A frequency tuning of 2% was also achieved with a tuning voltage of 50 V. This work showed many promising results for the realization of a micromechanical filter. However, much improvement is still needed, such as the central frequency, which needs to be increased for many applications, and the biasing voltage, which needs to be decreased for all applications.

In order to push the resonance frequency of a mechanical resonator higher, researchers have been pushing the limits of microfabrication technology to further down-scale mechanical dimensions to nanometre scale. Using electron beam lithography and various state of the art reactive etching techniques, fixed–fixed single-crystal silicon beam resonators have been demonstrated with a beam width of 200 nm and a length of 10 μm [94]. A fundamental resonant frequency of 14 MHz was demonstrated with a Q of 2500 at milliTorr pressure and room temperature. A more recent demonstration by Cleland and Roukes [91] was carried out on a similar fixed–fixed single-crystal silicon beam resonator with dimensions of 7.7 μm in length, 0.33 μm in width, and 0.8 μm in height. Resonators of these nanometre dimensions were tested under an applied B field with a network analyser detecting the motion caused by the Lorentz force. A resonator

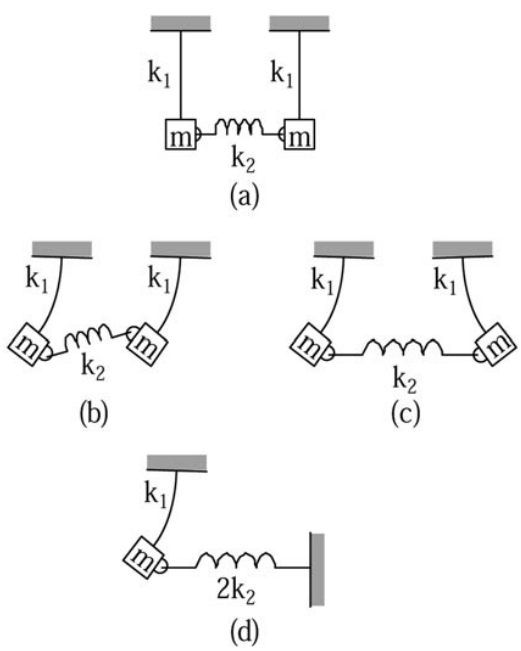

Figure 46. (a) Two identical spring–mass resonators with a coupling spring hinged between the two systems. The (b) in-phase and (c) out-of-phase resonance modes are illustrated, with (d) an equivalent model of the out-of-phase mode.

Q of 18 000 was measured in vacuum at 4.2 K with a fundamental resonant frequency of 70.72 MHz, one of the highest fundamental mechanical resonant frequencies demonstrated using MEMS technology. However, these

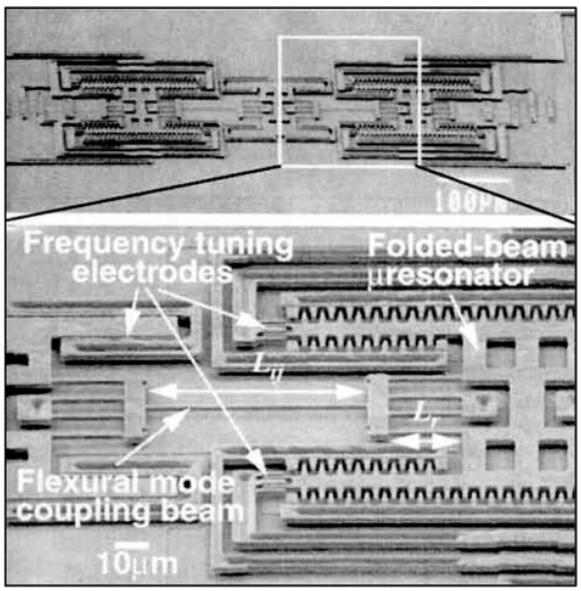

Figure 47. A 300 kHz micromechanical filter using three mechanically coupled resonators (from [85], University of Michigan).

nanometre scaled resonators require fine lithographic tools often not readily accessible to other researchers.

MEMS bandpass filters based on the fixed–fixed beam resonator design were first demonstrated in 1997 using a two-resonator design coupled *electrically* [86] as opposed to the common mechanical coupling in a mechanical filter. The central frequency was raised to 14.5 MHz with a Q of approximately 1000 at a pressure of 23 mTorr, and a dc biasing voltage requirement of 40 V. The insertion loss was measured to be 13.4 dB. In comparison with the earlier 300 kHz using three resonators mechanically coupled together [85], the central frequency of this fixed–fixed beam resonator based filter is raised and the dc bias voltage is lowered to 40 V, both of which still have room for further improvement. The insertion loss and Q also need some improvement, but the overall achievement of a higher resonant frequency than its macroscopic counterparts is very promising. There is, on the other hand, one rule of significant importance in a mechanical filter that this design has violated, that is, the use of an electrical coupling mechanism. In comparison to a pure mechanical filter, filter parameters, such as the signal-to-noise ratio, linearity, and stability, are all at risk when electronics are used in coupling mechanical resonators.

Mechanical coupling was used shortly after the initial filter demonstration in [86] in place of the electrical coupling in this fixed–fixed beam resonator based mechanical filter [95]. Figure 48 shows a schematic representation, an equivalent circuit diagram, a SEM image, and the transmission spectrum of such a two fixed–fixed beam resonator based filter with a low-velocity mechanical coupling spring. The resonating beams are made out of polysilicon thin film with dimensions of 8 μm in width, 22 μm in length, and 2 μm in thickness. The mechanical coupling beam between the two resonators is 11.8 μm long, and the gap between the resonating beams and the bottom electrodes is 25 nm. This mechanical filter has a central frequency of 34.5 MHz, one of the highest for a MEMS-based mechanical filter. Results include an insertion loss of less than 6 dB, a rejection of 25 dB, and a bandwidth of 460 kHz. A dc bias of 15 V is required for the operation.

As the physical dimensions scale down further, while simultaneously pushing the mechanical filter frequencies higher, the clamping loss in a fixed–fixed beam resonator becomes a significant and limiting factor of the resonator's Q. A silicon beam thickness and width of 2 μm each would require a beam length of less than 5 μm to achieve a resonating frequency of a few 100 megahertz. In such a case, the 'beam' is more like a 'block', and the boundary conditions at the clamps are thus extremely important and challenging. An alternative resonator design using a free–free beam structure has been demonstrated [90]. Figure 49 shows such a resonator. The device is a torsional resonator with two torsional beams supported at its flexural *node* points. The torsional beams are anchored to the substrate at each end, and are designed to have a length equal to a quarter of the wavelength, so that the free–free beam sees zero impedance into the supports. This configuration minimizes the effect from the clamping loss at the anchoring points of the supporting torsional beams. A higher Q can thus be achieved. With the dimensions shown in figure 49, a resonant frequency of 70.95 MHz has been demonstrated with a Q of the order of 8000. A dc biasing voltage of about 98 V is required. With this approach, resonators with a resonant frequency as high as 92.25 MHz have been demonstrated. Multi-resonator filters using these free–free resonators have not yet been demonstrated.

MEMS-based mechanical resonators and filters have shown promising characteristics in achieving important filter parameters, such as narrow bandwidth, low loss, and good stability. However, as the dimensions become smaller and smaller in most of the MEMS devices, the electromechanical coupling coefficient linking the electrical and mechanical sides of a transducer must be kept in mind as another important design parameter. This coefficient is often defined as the ratio of the energy stored in the mechanical system to the total input energy. As the physical dimensions become smaller, the gap sustaining the electrical signal power is also smaller. Some air gaps in the examples are less than 100 nm. The signal power handling capability of a micromechanical filter is thus another design parameter to keep in mind. Also, the output electrical impedance of a micromechanical device may become fairly high, due to the smaller capacitance of the resonator as a part of the down-scaling. Parasitic and load reactance can thus alter the filter's spectrum characteristics, and must be taken into careful consideration. The last, and by no means the least, important item for a mechanical filter is the device packaging. Hermeticity is a key parameter in keeping the high-Q value of the resonators and their long-term stability. Unlike other RF MEMS components that separate electrical and mechanical domains *to first order*, mechanical resonators and filters rely on their mechanical characteristics to produce the desired electrical functions. The 'mechanical Q' in an electromechanical filter, for example, is also the 'electrical Q'. This intimacy between the mechanical and electrical

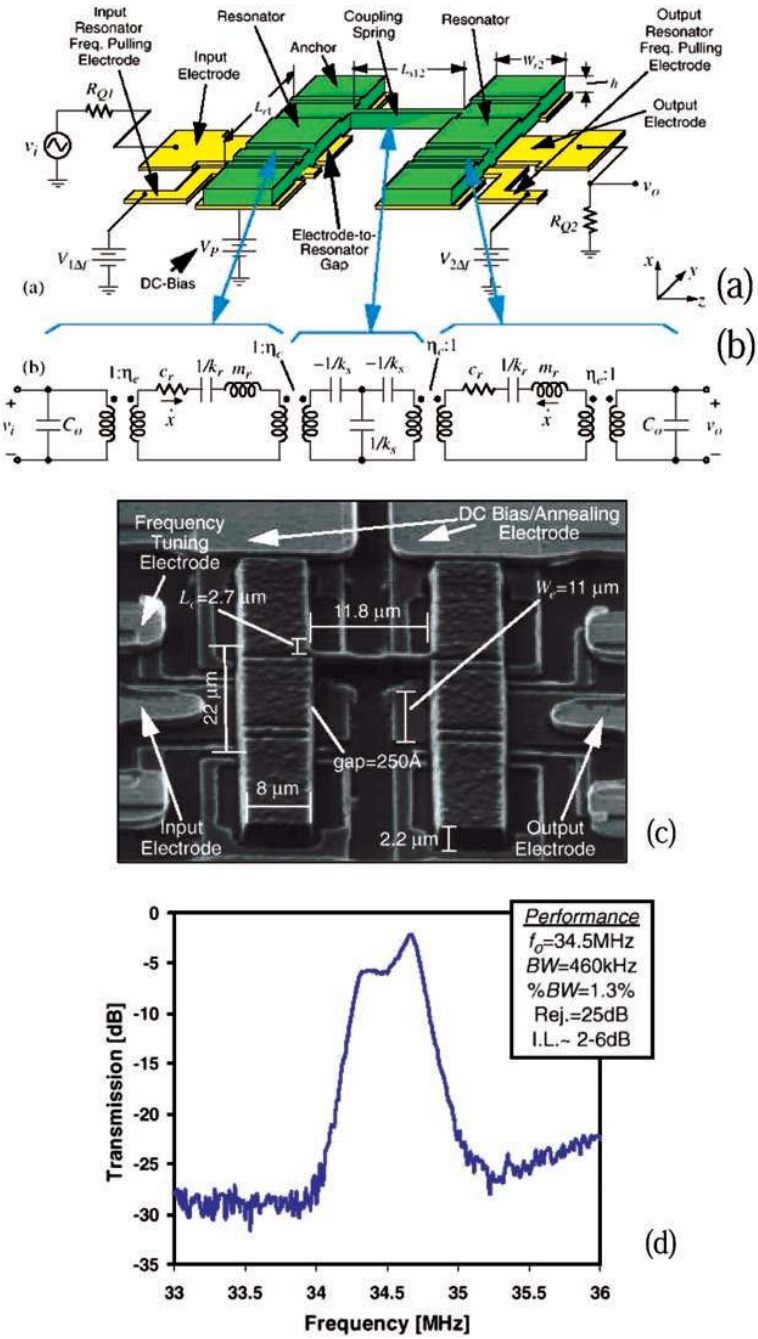

Figure 48. A 34.5 MHz fixed–fixed beam resonator based micromechanical filter: (a) schematic representation, (b) an equivalent circuit diagram, (c) a SEM micrograph and (d) a transmission spectrum (from [85], University of Michigan).

domains challenges the engineering of micromechanical resonators and filters, and on the other hand, provides the basis for the excellent performances of the same devices.

7. MEMS-based microwave and millimetre wave elements

At high frequency, substrate losses become significant. As MEMS and micromachining technologies became available, the obvious and the first thing researchers did was to remove portions of the lossy substrate material surrounding a microwave component, very similar to the suspended high-Q spiral inductors. Demonstrations have been performed with the microwave devices enclosed in a metallized cavity [96] and the top air cavity created by anisotropic etching of a low-resistivity silicon wafer in ethylene diamine pyrocatechol (EDP) solution. The etched surface is then metallized to provide a ground shield. A second silicon wafer, on which the microwave devices are first fabricated, is also etched in EDP from the back side of the wafer, leaving a silicon cavity surrounded by etched grooves. The back side of this wafer is then metallized to provide a ground shield for the bottom silicon cavity. The two wafers are then adhesively bonded, resulting in the microwave devices being completely shielded

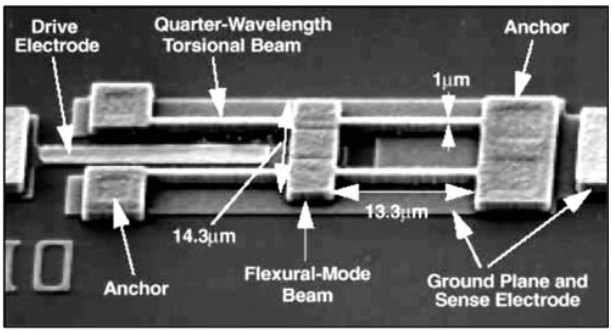

Figure 49. A 70.95 MHz free–free torsional beam resonator (from [90], University of Michigan).

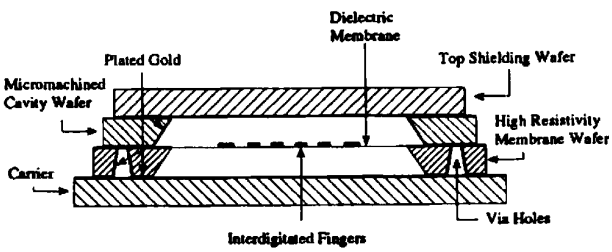

Figure 50. A schematic cross sectional illustration of the cavity technology developed by Chi and Rebeiz (from [100], University of Michigan).

in a cavity environment. Since the bottom half of the cavity is made of silicon, a high-resistivity silicon wafer was used for the bottom wafer to minimize losses in the lower silicon cavity. This technology has provided a useful and cost-effective way of minimizing substrate losses for microwave components, and has been adapted to demonstrate a number of microwave components including a stepped-impedance lowpass filter [96–98] with a 3 dB point of 19 GHz, microstrip antennae, and a conformal microwave packaging scheme [97, 99].

A similar micromachined cavity technology was reported in 1995 with four wafers stacked, as shown in figure 50 [100]. The top and bottom wafers serve as ground shields, and the middle two wafers create the top and bottom air cavities, with the microwave components sandwiched in the middle. Note that the bottom cavity is also air, as opposed to the silicon used in the earlier technology. An interdigitated bandpass filter with grounded coplanar waveguide (GCPW) transmission lines was designed and fabricated to demonstrate this micromachining technology. The filter dimensions, along with an image of the interdigitated filter, are shown in figure 51(a), with the filter response shown in figure 51(b) [100]. Results include an insertion loss of 1.7 dB at a central frequency of 20.3 GHz (including 0.6 dB from the two GCPW transmission lines) with a 3 dB bandwidth of 3.1 GHz, and a return loss of better than −15 dB in the passband. Other microwave devices were also demonstrated, including Lange couplers and single-sideband mixers [101], stripline resonators, various other lowpass and bandpass filters [102], and distributed MEMS phase shifters [103].

MEMS and micromachining technology has also been applied to millimetre-wave cavity resonator applications. This is an effort to minimize phase noise by improving

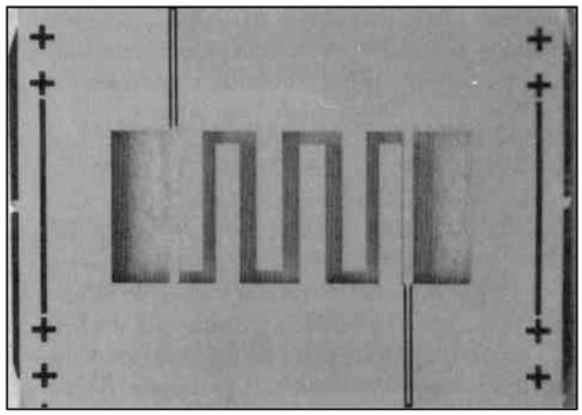

K	$s_{k,k+1}(\mu m)$	K	$w_k(\mu m)$	$L_k(\mu m)$
0, 6	22.9	0, 7	228.6	3373.1
1, 5	284.5	1, 6	502.9	3111.5
2, 4	370.8	2, 5	528.3	3101.3
3	375.9	3, 4	576.6	3086.1
K: finger number			w_k: finger width	
$s_{k,k+1}$: gap between fingers			L_k: finger length	

(a)

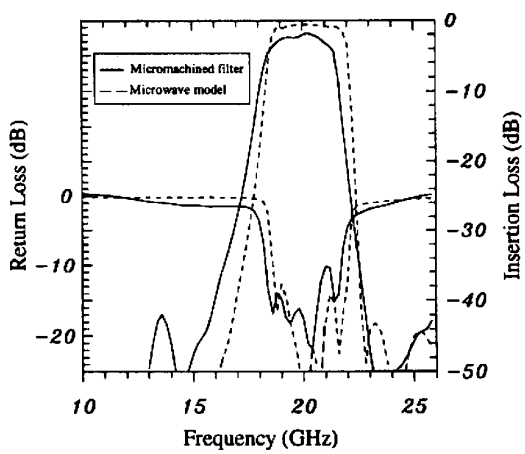

(b)

Figure 51. (a) An interdigitated bandpass filter is shown with dimensions (b) and its response. The cavity technology shown in figure 50 is used for this filter demonstration (from [100], University of Michigan).

resonator Q in comparison with on-chip microstrip-type resonators, as the phase noise is inversely proportional to the square of Q. A 30 GHz cavity resonator was demonstrated by Kim *et al* [104] in 1999 with a Q of 120 and a phase noise improvement of more than 10 dBc Hz^{-1}. At the same time, MEMS is also being used to address other aspects of the microwave and millimetre-wave field, including tunability, high-power applications, and quasi-optic beam steering and combining. Kudrle *et al* [105] demonstrated a millimetre-wave phase shifter that has a *continuous* tuning or shifting capability. Ground–signal transmission lines are fabricated using high-resistivity single-crystal substrate silicon with a DRIE technique. Figure 52 shows a portion of such transmission lines in a 30 GHz stepped-impedance lowpass filter [105]. These transmission lines are attached to on-chip comb-drive actuators so that the transmission line spacing

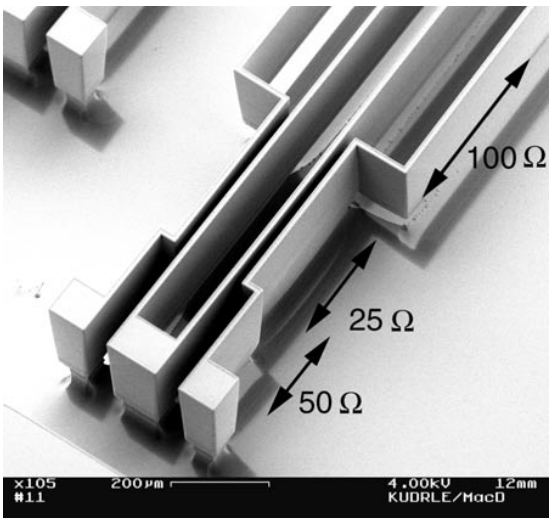

Figure 52. Metallized single-crystal silicon transmission lines (50 μm in height) as a part of a 30 GHz stepped-impedance lowpass filter (from [105], Cornell University).

can be electromechanically and continuously adjusted by applying a voltage on the comb-drive actuators. This adjustment results in a change in the impedance of a short transmission line that can be modelled as a lumped shunt capacitor, and can be used for the phase shifting functionality. A maximum phase shift of 48° at a frequency of 48 GHz was achieved using a drive voltage of 45 V. The insertion loss was less than 1.8 dB.

For high-power microwave applications, microstrip transmission lines and filters have been demonstrated on a fused quartz substrate using the LIGA process [106], a German acronym for lithography, electroplating and moulding. Metal films between 10 and 500 μm in thickness were plated to form the transmission lines with a substrate thickness of 420 μm. This thick metal structure makes possible high-power applications. Transmission lines, as well as lowpass and bandpass microwave filters, have been fabricated using this process technology and characterized [106]. Alternatively, for high-power applications, millimetre waves can be treated as quasi-optic beams, where micromachined apertures can be formed to steer and combine the propagating millimetre waves [107]. This method of beam steering was demonstrated at 90 GHz in [107]. Periodic and metallized rhombic waveguides with ⟨111⟩ walls were formed in silicon substrates using an anisotropic etchant (KOH). A micromachined switch was formed on a dielectric membrane in each of the waveguides. When the switches are closed, the metal pattern on the membrane represents a shunt inductive reactance; and when the switches are open, a shunt capacitive reactance. Therefore, by controlling the switch state, a phase shift can be introduced to the propagating wave. The whole structure requires 10 stacked layers in order to create a 360° phase shift. By changing the settings of the switches in different layers, different phase shifts can be achieved.

These are a few examples of MEMS for microwave and millimetre-wave applications. Long-time issues, such as substrate parasitics and losses, microwave packaging, tunability, and high-power microwave systems, are being addressed with the MEMS technology. Superb results have been demonstrated. This is just a beginning for the revolutionary MEMS technology for microwave and millimetre-wave applications.

8. Conclusions

The recent progress in RF MEMS was reviewed in this paper from a device perspective. Devices reviewed include switches and relays, tunable capacitors, integrated inductors, mechanical resonators and filters, and some microwave and millimetre-wave components. Important device parameters were highlighted, as they make significant contributions to the performance of the final products in which the devices are used. The insertion loss, isolation, linearity, quality factor, and the self-resonance frequency are just a few of these important device parameters. Excellent insertion loss and isolation parameters have been observed in MEMS RF switches and relays. Large tuning ratios in excess of 200% have been demonstrated for MEMS tunable capacitors with promising linearity performance. Q factors comparable to those of discrete components have also been demonstrated in integrated micromachined inductors. When filter applications, especially below 100 MHz, are in focus, micromechanical resonator based mechanical filters have been demonstrated with superb performance parameters and a typical Q in the 1000s. MEMS technologies applied to microwave and millimetre-wave applications for parasitic removal have also shown large performance benefits without cost increases. Challenges and statuses of these RF MEMS devices were outlined and discussed, with an extremely promising future from an overview perspective of the RF MEMS field. The intent of this topical review paper is to provide perspectives to newcomers in the field, and empower potential end-users with an overall device picture, current status, and a vision of their ultimate performance capabilities. When evaluating various RF MEMS technologies and publications, I strongly urge the readers to keep in mind that the overall MEMS field is not much more than 10 years old, and the RF MEMS field has really been shaped within the past five or six years. The future should be bright and unlimited.

Acknowledgments

Thanks are due to the members of the RSC clean room support staff in the area of micromachining and the various MEMS processing technology developments. Furthermore, I would like to acknowledge valuable contributions from many colleagues to the work presented here, and in particular Sangtae Park, Bob Anderson, Patti Richardson, Jeff DeNatale, Hank Marcy, Rob Mihailovich, Judy Studer, Rob Borwick, Jim Waldrop and Ann Wang.

References

[1] Petersen K E 1982 Silicon as a mechanical material *Proc. IEEE* **70** 420–57

[2] Chau K H-L, Lewis S R, Zhao Y, Howe R T, Bart S F and Marcheselli R G 1995 An integrated force-balanced capacitive accelerometer for low-g applications *Tech. Digest, 8th Int. Conf. on Solid-State Sensors and Actuators* pp 593–6

[3] Burns D W, Horning R D, Herb W R, Zook J D and Guckel H 1995 Resonant microbeam accelerometers *Tech. Digest, 8th Int. Conf. on Solid-State Sensors and Actuators* pp 659–62
[4] Chavan A V and Wise K D 1997 A batch-processed vacuum-sealed capacitive pressure sensor *Tech. Digest, 1997 Int. Conf. on Solid-State Sensors and Actuators* pp 1449–52
[5] Lee S-S, Motamedi E and Wu M C 1997 Surface-micromachined free-space fiber optic switches with integrated microactuators for optical fiber communication systems *Tech. Digest, 1997 Int. Conf. on Solid-State Sensors and Actuators* pp 85–8
[6] Chen J and Wise K 1995 A high-resolution silicon monolithic nozzle array for inkjet printing *Tech. Digest, 8th Int. Conf. on Solid-State Sensors and Actuators* pp 321–4
[7] Petersen K E 1979 Micromechanical membrane switches on silicon *IBM J. Res. Dev.* **23** 376–85
[8] Hosaka H, Kuwano H and Yanagisawa K 1994 Electromagnetic microrelays: concepts and fundamental characteristic *Sensors Actuators* A **40** 41–7
[9] Taylor W P, Allen M G and Dauwalter C R 1997 Batch fabricated electromagnetic microrelays *Proc. 45th Relay Conf.* pp 8.1–8.6
[10] Taylor W P and Allen M G 1997 Integrated magnetic microrelays: normally open, normally closed, and multi-pole devices *Tech. Digest, 1997 Int. Conf. on Solid-State Sensors and Actuators* pp 1149–52
[11] Tilmans H A C *et al* 1999 A fully-packaged electromagnetic microrelay *Tech Digest, 12th IEEE Int. Conf. on Micro Electro Mechanical Systems* pp 25–30
[12] Wright J A and Tai Y-C 1999 Magnetostatic MEMS relays for the miniaturization of brushless DC motor controllers *Tech. Digest, 12th IEEE Int. Conf. on Micro Electro Mechanical Systems* pp 594–9
[13] Grétillat M-A, Grétillat F and de Rooij N F 1999 Micromechanical relay with electrostatic actuation and metallic contacts *J. Micromech. Microeng.* **9** 324–31
[14] Sanders C 1998 MCNC thermally actuated microrelays *News Release* MEMS Technology Application Center MCNC, November 30
[15] Larson L E, Hackett R H and Lohr R F 1991 Microactuators for GaAs-based microwave integrated circuits *Tech. Digest, 6th Int. Conf. on Solid-State Sensors and Actuators* pp 743–6
[16] Yao J J and Chang M F 1995 A surface micromachined miniature switch for telecommunications applications with signal frequencies from DC up to 4 GHz *Tech. Digest, 8th Int. Conf. on Solid-State Sensors and Actuators* pp 384–7
[17] Schiele I, Huber J, Evers C, Hillerich B and Kozlowski F 1997 Micromechanical relay with electrostatic actuation *Tech. Digest, Int. Conf. on Solid-State Sensors and Actuators* pp 1165–8
[18] De Los Santos H J, Kao Y-H, Caigoy A L and Ditmars E D 1997 Microwave and mechanical considerations in the design of MEM switches for aerospace applications *Proc. IEEE Aerospace Conf.* vol 3, pp 235–54
[19] Hyman D *et al* 1999 Surface-micromachined RF MEMS switches on GaAs substrates *Int. J. RF Microwave CAE* **9** 348–61
[20] Hyman D *et al* 1999 GaAs-compatible surface-micromachined RF MEMS switches *Electron. Lett.* **35** 224–6
[21] Zavracky P M, Majumder S and McGruer N E 1997 Micromechanical switches fabricated using nickel surface micromachining *IEEE J. MEMS* **6** 3–9
[22] Majumder S, McGruer N E, Zavracky P M, Adams G G, Morrison R H and Krim J 1997 Measurement and modeling of surface micromachined, electrostatically actuated microswitches *Tech. Digest, 1997 Int. Conf. on Solid-State Sensors and Actuators* pp 1145–8
[23] McGruer N E, Zavracky P M, Majumder S, Morrison R H and Adams G G 1998 Electrostatically actuated microswitches; scaling properties *Tech. Digest, Solid State Sensor and Actuator Workshop* pp 132–5
[24] Schlaak H F, Arndt F and Hanke M 1997 Silicon-microrelay—a small signal relay with electrostatic actuator *Proc 45th Relay Conf.* pp 10.1–10.7
[25] Suzuki K, Chen S, Marumoto T, Ara Y and Iwata R 1999 A micromachined RF microswitch applicable to phased-array antennas *Tech. Digest, IEEE Microwave Theory Techniques Symp.* pp 1923–6
[26] Sovero E A, Mihailovich R, Deakin D S, Higgins J A, Yao J J, DeNatale J F and Hong J H 1999 Monolithic GaAs PHEMT MMICs integrated with high performance MEMS microrelays *Proc. IMOC'99 (Rio de Janeiro, Brazil)*
[27] Muldavin J B and Rebeiz G M 1999 30 GHz tuned MEMS switches *Tech. Digest, IEEE Microwave Theory and Techniques Symp.* pp 1511–14
[28] Goldsmith C, Lin T-H, Powers B, Wu W-R and Norvell B 1995 Micromechanical membrane switches for microwave applications *Tech. Digest, IEEE Microwave Theory and Techniques Symp.* pp 91–4
[29] Goldsmith C, Randall J, Eshelman S, Lin T-H, Denniston D, Chen S and Norvell B 1996 Characteristics of micromachined switches at microwave frequencies *Tech. Digest, IEEE Microwave Theory and Techniques Symp.* pp 1141
[30] Yao Z J, Chen S, Eshelman S, Denniston D and Goldsmith C 1999 Micromachined low-loss microwave switches *IEEE J. MEMS* **8** 129–34
[31] Pacheco S, Nguyen C T and Katehi L P B 1998 Micromachined electrostatic K-band switches *Tech. Digest IEEE MTT-S Int. Microwave Symp.* pp 1569–72
[32] Sakata M, Komura Y, Seki T, Kobayashi K, Sano K and Horiike S 1999 Micromachined relay which utilizes single crystal silicon electrostatic actuator *Tech. Digest, 12th IEEE Int. Conf. on Micro Electro Mechanical Systems* pp 21–4
[33] Hiltmann K M, Schmidt B, Sandmaier H and Lang W 1997 Development of micromachined switches with increased reliability *Tech. Digest, 1997 Int. Conf. on Solid-State Sensors and Actuators* pp 1157–60
[34] Drake J, Jerman H, Lutze B and Stuber M 1995 An electrostatically actuated micro-relay *Tech. Digest, 8th Int. Conf. on Solid-State Sensors and Actuators* pp 380–3
[35] Admschik M, Ertl S, Schmid P, Gluche P, Flöter A and Kohn E 1999 Electrostatic diamond micro switch *Tech. Digest, 10th Int. Conf. on Solid-State Sensors and Actuators* pp 1284–7
[36] Grétillat M-A, Thiébaud P, Linder C and de Rooij N F 1995 Integrated circuit compatible polysilicon microrelays *J. Micromech. Microeng.* **5** 156–60
[37] Simon J, Saffer S and Kim C-J 1996 A micromechanical relay with a thermally-driven mercury micro-drop *Proc. IEEE, 9th Ann. Int. Workshop on Micro Electro Mechanical Systems* pp 515–20
[38] Saffer S, Simon J and Kim C-J 1996 Mercury-contact switching with gap-closing microcantilever *Proc. SPIE* **2882** 204–8
[39] Sun X-Q, Farmer K R and Carr W N 1998 A bistable microrelay based on two-segment multimorph cantilever actuators *Proc. IEEE, 11th Ann. Int. Workshop on Micro Electro Mechanical Systems* pp 154–9
[40] Kruglick E J J and Pister K S J 1998 Bistable MEMS relays and contact characterization *Tech. Digest, Solid State Sensor and Actuator Workshop* pp 333–7
[41] Schiele I and Hillerich B 1999 Comparison of lateral and vertical switches for application as microrelays *J. Micromech. Microeng.* **9** 146–50
[42] Kruglick E J J and Pister K S J 1999 Lateral MEMS microcontact considerations *IEEE J. MEMS* **8** 264–71

[43] Grétillat M-A, Yang Y-J, Hung E S, Rabinovich V, Ananthasuresh G K, de Rooij N F and Senturia S D 1997 Nonlinear electromechanical behavior of an electrostatic microrelay *Tech. Digest, 1997 Int. Conf. on Solid-State Sensors and Actuators* pp 1141–4
[44] Gopinath A and Rankin J B 1985 GaAs FET RF switches *IEEE Trans. Electron Devices* **32** 1272–8
[45] Caverly R H 1993 Distortion in arsenide MESFET switches *IEEE Trans. Microwave Theor. Techniq.* **41** 1323–8
[46] Ota Y, Sakakura M, Fujimoto K, Yamamoto S and Fujimoto H 1995 High isolation and low insertion loss switch IC using GaAs MESFET's *IEEE Trans. Microwave Theor. Technol.* **43** 2175–7
[47] Kobayashi K W, Oki A K, Umemoto D K, Claxton S K Z and Streit D C 1993 Monolithic GaAs HBT p–I–n diode variable gain amplifiers, attenuators, and switches *IEEE Trans. Microwave Theor. Techniq.* **41** 2295–302
[48] Schimkat J 1998 Contact materials for microrelays *Proc. IEEE, 11th Ann. Int. Workshop on Micro Electro Mechanical Systems* pp 190–4
[49] Seki T, Sakata M, Nakajima T and Matsumoto M 1997 Thermal buckling actuator for micro relays *Tech. Digest, 1997 Int. Conf. on Solid-State Sensors and Actuators* pp 1153–6
[50] Yao J J, DeNatale J, Erlandson R, Mihailovich R, Park S, Anderson R, Langridge R and Anderson G 1999 Micromachined RF switches and tunable capacitors for higher performance secure communications systems *DARPA Principal Investigators Meeting*
[51] Brown E R 1998 RF-MEMS switches for reconfigurable integrated circuits *IEEE Trans. Microwave Theor. Technol.* **46** 1868–80
[52] Soyuer M, Jenkins K E, Burghartz J N and Hulvey M D 1996 A 3 V 4 GHz nMOS voltage-controlled oscillator with integrated resonator *Tech. Digest, IEEE Int. Solid-State Circuit Conf.* pp 394–5
[53] Kim D-W and Kwon Y-S 1996 Photoresponse of area-variable varactor diode *Electron. Lett.* **32** 466–7
[54] Larson L E, Hackett R H, Melendes M A and Lohr R F 1991 Micromachined microwave actuator (MIMAC) technology—a new tuning approach for microwave integrated circuits *Tech. Digest, IEEE Microwave and Millimeter-Wave Monolithic Circuits Symp.* pp 27–30
[55] Young D J and Boser B E 1996 A micromachined variable capacitor for monolithic low-noise VCOs *Tech. Digest, Solid State Sensor and Actuator Workshop* pp 86–9
[56] Young D J, Malba V, Ou J J, Bernhardt A F and Boser B E 1998 A low-noise RF voltage-controlled oscillator using on-chip high-Q three-dimensional coil inductor and micromachined variable capacitor *Tech. Digest, Solid State Sensor and Actuator Workshop* pp 128–31
[57] Young D J, Tham J L and Boser B E 1999 Voltage-controlled oscillator for wireless communications *Tech. Digest, 10th Int. Conf. on Solid-State Sensors and Actuators* pp 1386–9
[58] Dec A and Suyama K 1997 Micromachined varactor with wide tuning range *Electron. Lett.* **33** 922–4
[59] Dec A and Suyama K 1999 A 2.4 GHz CMOS LC VCO using micromachined variable capacitors for frequency tuning *Tech. Digest, IEEE Microwave Theory and Techniques Symp.* pp 79–82
[60] Yao J J, Park S and DeNatale J 1998 High tuning-ratio MEMS-based tunable capacitors for RF communications applications *Tech. Digest, Solid State Sensor and Actuator Workshop* pp 124–7
[61] Hung E and Senturia S 1998 Tunable capacitors with programmable capacitance–voltage characteristic *Tech. Digest, Solid State Sensor and Actuator Workshop* pp 292–5
[62] Park J-H, Kim H-T, Kwon Y and Kim Y-K 1999 A tunable millimeter-wave filter using coplanar waveguide and micromachined variable capacitors *Tech. Digest, 10th Int. Conf. on Solid-State Sensors and Actuators* pp 1272–5
[63] Goldsmith C L, Malczewski A, Yao Z J, Chen S, Ehmke J and Hinzel D H 1999 RF MEMS variable capacitors for tunable filters *Int. J. RF Microwave Comput.-Aided Eng.* **9** 362–74
[64] Feng Z, Zhang W, Su B, Harsh K F, Gupta K C, Bright V and Lee Y C 1999 Design and modeling of RF MEMS tunable capacitors using electro-thermal actuators *Tech. Digest, 1999 IEEE MTT-S Int. Microwave Symp.* pp 1507–10
[65] Chen C-L and Yao J J 1996 Damping control of MEMS devices using structural design approach *Tech. Dig, Solid State Sensor and Actuator Workshop* pp 72–5
[66] Koester D A, Mahadevan R, Shishkoff A and Markus K W 1996 *Smart-MUMPs Design Handbook Including MUMPs Introduction and Design Rules* rev 4, MEMS Technology Application Center MCNC, pp 1–8
[67] Harsh K F, Zhang W, Bright V M and Lee Y C 1999 Flip-chip assembly for Si-based RF MEMS *Proc. IEEE, 12th Ann. Int. Workshop on Micro Electro Mechanical Systems* pp 273–8
[68] HPFZ Division, Unisil Corporation 1999 High purity float zone wafer capabilities 401 National Avenue, Mountain View, CA 94043, USA
[69] Lovelace D, Camilleri N and Kannel G 1994 Silicon MMIC inductor modeling for high volume, low cost applications *Microwave J.* August 60–71
[70] Arcioni P, Castello R, Perregrini L, Sacchi E and Svelto F 1999 An innovative modelization of loss mechanism in silicon integrated inductors *IEEE Trans. Circuits Syst.* II **46** 1453–60
[71] Chang J Y-C, Abidi A A and Gaitan M 1993 Large suspended inductors on silicon and their use in a 2 μm CMOS RF amplifier *IEEE Electron. Device Lett.* **14** 246–8
[72] Rofougaran A, Chang J Y-C, Rofougaran M and Abidi A A 1996 A 1 GHz CMOS RF front-end IC for a direct-conversion wireless receiver *IEEE J. Solid-State Circuits* **31** 880–9
[73] Fan L, Chen R T, Nespola A and Wu M C 1998 Universal MEMS platforms for passive RF components: suspended inductors and variable capacitors *Proc. IEEE, 11th Ann. Int. Workshop on Micro Electro Mechanical Systems* pp 29–33
[74] Ziaie B, Kocaman N K and Najafi K 1997 A generic micromachined silicon platform for low-power, low-loss miniature transceivers *Tech. Digest, 1997 Int. Conf. on Solid-State Sensors and Actuators* pp 1153–6
[75] Ahn C H and Allen M G 1993 A planar micromachined spiral inductor for integrated magnetic microactuator applications *J. Micromech. Microeng.* **3** 37–44
[76] Ahn C H, Kim Y J and Allen M G 1994 A fully integrated planar toroidal inductor with a micromachined nickel–iron magnetic bar *IEEE Trans. Components Packaging Manufact. Technol.* A **17** 463–9
[77] Sullivan C R and Sanders S R 1996 Design of microfabricated transformers and inductors for high-frequency power conversion *IEEE Trans. Power Electron.* **11** 228–38
[78] Daniel L, Sullivan C R and Sanders S R 1999 Design of microfabricated inductors *IEEE Trans. Power Electron.* **14** 709–23
[79] Yoon J-B, Han C-H, Yoon E and Kim C-K 1999 High-performance three-dimensional on-chip inductors fabricated by novel micromachining technology for RF MMIC *Tech. Digest 1999 IEEE MTT-S Int. Microwave Symp.* pp 1523–6
[80] Zhou S, Sun X-Q and Carr W N A 1999 Monolithic variable inductor network using microrelays with combined thermal and electrostatic actuation *J. Micromech. Microeng.* **9** 45–50
[81] Adler R 1947 Compact electromechanical filters *Electronics* **20** 100–5
[82] Johnson R A 1983 *Mechanical Filters in Electronics* (New York: Wiley) ISBN 0-471-08919-2

[83] Tang W C, Nguyen T-C H and Howe R T 1989 Laterally driven polysilicon resonant microstructures *Sensors Actuators* **20** 25–32

[84] Lin L, Nguyen C T-C, Howe R T and Pisano A P 1992 Micro electromechanical filters for signal processing *Proc. IEEE, 5th Ann. Int. Workshop on Micro Electro Mechanical Systems* pp 226–31

[85] Wang K and Nguyen C T-C 1997 High-order micromechanical electronic filters *Proc. IEEE, 10th Ann. Int. Workshop on Micro Electro Mechanical Systems* 25–30

[86] Clark J R, Bannon F D III, Wong A-C and Nguyen C T-C 1997 Parallel-resonator HF micromechanical bandpass filters *Tech. Digest, 1997 Int. Conf. on Solid-State Sensors and Actuators* pp 1161–4

[87] Katehi L P B, Rebeiz G M and Nguyen C T-C 1998 MEMS and Si-micromachined components for low-power, high-frequency communications systems *Tech. Digest, IEEE MTT-S Int. Microwave Symp.* pp 331–3

[88] Wong A-C, Clark J R and Nguyen C T-C 1999 Anneal-activated, tunable, 68 MHz micromechanical filters *Tech. Digest, 10th Int. Conf. on Solid-State Sensors and Actuators* pp 1390–3

[89] Wang K, Wong A-C, Hsu W-T and Nguyen C T-C 1997 Frequency trimming and Q-factor enhancement of micromechanical resonators via localized filament annealing *Tech. Digest, 1997 Int. Conf. on Solid-State Sensors and Actuators* pp 109–12

[90] Wang K, Yu Y, Wong A-C and Nguyen C T-C 1999 VHF free–free beam high-Q micromechanical resonators *Proc. IEEE, 12th Ann. Int. Workshop on Micro Electro Mechanical Systems* pp 453–8

[91] Cleland A N and Roukes M L 1996 Fabrication of high frequency nanometer scale mechanical resonators from bulk Si substrates *Appl. Phys. Lett.* **69** 2653–5

[92] Cleland A N and Roukes M L 1999 External control of dissipation in a nanometer-scale radio frequency mechanical resonator *Sensors Actuators* A **72** 256–61

[93] Greywall D S 1999 Micromechanical RF filters excited by the Lorentz force *J. Micromech. Microeng.* **9** 78–84

[94] McMillan J A, Yao J J, Arney S C and MacDonald N C 1991 High frequency single crystal silicon resonant devices *Proc 38th Ann. Symp. and Topical Conf. of the American Vacuum Society*

[95] Nguyen C T-C, Wong A-C and Ding H 1999 Tunable, switchable, high-Q VHF microelectromechanical bandpass filters *Proc IEEE Int. Solid-State Circuit Conf.*

[96] Drayton R F and Katehi L P B 1994 Development of miniature microwave circuit components using micromachining techniques *Tech. Digest, 1994 IEEE MTT-S Int. Microwave Symp.* pp 225–8

[97] Drayton R F and Katehi L P B 1995 Micromachined conformal packages for microwave and millimeter-wave applications *Tech. Digest, 1995 IEEE MTT-S Int. Microwave Symp.* pp 1387–90

[98] Weller T M and Katehi L P B 1996 A millimeter wave micromachined lowpass filter using lumped elements *Tech. Digest, 1996 IEEE MTT-S Int. Microwave Symp.* pp 631–4

[99] Drayton R F, Henderson R M and Katehi L P B 1996 Advanced monolithic packaging concepts for high performance circuits and antennas *Tech. Digest, 1996 IEEE MTT-S Int. Microwave Symp.* pp 1615–18

[100] Chi C-Y and Rebeiz G M 1995 A low-loss 20 GHz micromachined bandpass filter *Tech. Digest, 1995 IEEE MTT-S Int. Microwave Symp.* pp 1531–4

[101] Chi C-Y and Rebeiz G M 1997 Design of Lange-couplers and single-sideband mixers using micromachining techniques *IEEE Trans. Microwave Theor. Techniq.* **45** 291–4

[102] Rebeiz G M, Katehi L P B, Weller T M, Chi C-Y and Robertson S V 1997 Micromachined membrane filters for microwave and millimeter-wave applications *Int. J. Microwave Millimeter-Wave CAE* **7** 149–66

[103] Barker N S and Rebeiz G M 1998 Distributed MEMS true-time delay phase shifters and wide-band switches *IEEE Trans. Microwave Theory Techniq.* **46** 1881–90

[104] Kim C, Song I, Song C, Cheon C, Kwon Y and Lee S 1999 A micromachined cavity resonator for mm-wave oscillator applications *Tech. Digest, 10th Int. Conf. on Solid-State Sensors and Actuators* pp 1268–71

[105] Kudrle T D, Neves H P, Rodger D C and MacDonald N C 1999 A microactuated millimeter wave phase shifter *Tech. Digest, 10th Int. Conf. on Solid-State Sensors and Actuators* pp 1276–9

[106] Willke T L and Gearhart S S 1996 Novel micromachined LIGA microstrip transmission lines and filters *Tech. Digest, 1996 IEEE MTT-S Int. Microwave Symp.* pp 1189–92

[107] Chiao J-C and Rutledge D 1994 Microswitch beam-steering grid *Int. Conf. on Millimeter and Submillimeter Waves and Applications*